Monthly Notices
of the
ROYAL ASTRONOMICAL SOCIETY

MNRAS **476,** 1596–1613 (2018)
Advance Access publication 2018 February 5

doi:10.1093/mnras/sty269

Revealing the Faraday depth structure of radio galaxy NGC 612 with broad-band radio polarimetric observations

J. F. Kaczmarek,[1,2,3★] C. R. Purcell,[2,3] B. M. Gaensler,[2,4] X. Sun,[2,5] S. P. O'Sullivan[6] and N. M. McClure-Griffiths[7]

[1]*CSIRO Astronomy and Space Science, Australia Telescope National Facility, Box 76, Epping, NSW 1710, Australia*
[2]*Sydney Institute for Astronomy, School of Physics, The University of Sydney, NSW 2006 Australia*
[3]*Research Centre for Astronomy, Astrophysics, and Astrophotonics, Macquarie University, NSW 2109, Australia*
[4]*Dunlap Institute for Astronomy and Astrophysics, University of Toronto, 50 St George Street, Toronto, ON M5S 3H4, Canada*
[5]*Department of Astronomy, Yunnan University, and Key Laboratory of Astroparticle Physics of Yunnan Province, Kunming, 650091, China*
[6]*Hamburger Sternwarte, Universität Hamburg, Gojenbergsweg 112, Hamburg D-21029, Germany*
[7]*Research School of Astronomy and Astrophysics, Australian National University, Canberra, ACT 2611, Australia*

Accepted 2018 January 22. Received 2017 December 29; in original form 2017 November 20

ABSTRACT

We present full-polarization, broad-band observations of the radio galaxy NGC 612 (PKS B0131-637) from 1.3 to 3.1 GHz using the Australia Telescope Compact Array. The relatively large angular scale of the radio galaxy makes it a good candidate with which to investigate the polarization mechanisms responsible for the observed Faraday depth structure. By fitting complex polarization models to the polarized spectrum of each pixel, we find that a single polarization component can adequately describe the observed signal for the majority of the radio galaxy. While we cannot definitively rule out internal Faraday rotation, we argue that the bulk of the Faraday rotation is taking place in a thin skin that girts the polarized emission. Using minimum energy estimates, we find an implied total magnetic field strength of 4.2 μG.

Key words: techniques: polarimetric – galaxies: individual: NGC 612 – galaxies: magnetic fields – radio continuum: galaxies.

1 INTRODUCTION

The synchrotron emission associated with radio galaxy lobes can be used to dissect the evolutionary history of the host galaxy as well as that of the surrounding intergalactic medium. Jets that are launched from a central supermassive black hole create, and subsequently inflate, radio lobes (Begelman, Blandford & Rees 1984; Xu et al. 2010). As the lobes expand, they have the potential to interact with the surrounding environment, possibly implanting signatures from the interaction into the generated synchrotron plasma. Additionally, these interactions can enrich the surrounding medium with large amounts of energy and metals (Aguirre et al. 2001; Reuland et al. 2007; McNamara et al. 2009). However, the relative amount of thermal material present in radio lobes is poorly constrained, and it has been shown that the lobes are predominantly inflated with non-thermal, synchrotron-emitting plasma (Begelman et al. 1984). Evidence for thermal material distributed throughout the volumes of radio lobes has been argued in the case of some of the most well-studied radio galaxies, Centaurus A (O'Sullivan et al. 2012) and Fornax A (Fomalont et al. 1989). The key to detecting thermal material in radio lobes may lie in the detailed analysis of the Faraday depth structure, as the Faraday depth encodes the thermal electron density in addition to the line-of-sight magnetic field strength. Therefore, by studying the polarized emission associated with radio lobes we can gain insight towards the origin and density of thermal gas in radio galaxies and the surrounding intergalactic medium.

Differentiating between polarization contributions that are internal and those that are external to the source has proven difficult. The vast majority of investigations into the nature of large-scale polarization signatures associated with radio galaxies have found distributions that appear non-homogeneous (e.g. Bonafede et al. 2010; Govoni et al. 2010). The irregular distributions of Faraday depth structures have been largely attributed to the superposition of intervening material along the line of sight. Laing (1988), Kronberg et al. (2008), and Guidetti et al. (2010) successfully modelled rotation measures (RMs) associated with radio galaxies as a result of foreground emission from the large-scale, diffuse intracluster medium.

In contrast, other authors have argued that a significant portion of the observed RM is intrinsic to the radio lobe itself. In the latter case, there is even more debate as to where in the lobe the Faraday rotation takes place. Rudnick & Blundell (2003), Guidetti et al. (2011), and Guidetti et al. (2012) make the case that the Faraday rotating material forms a thin skin encompassing the purely synchrotron lobes, though later work by Ensslin et al. (2003) demonstrated

★ E-mail: jane.kaczmarek@csiro.au

limitations in the null experiment performed by Rudnick & Blundell (2003). In contrast, O'Sullivan et al. (2013) successfully fit their observations by modelling radio lobes as a mixture of relativistic synchrotron plasma and magnetized, thermal gas.

Each of the aforementioned scenarios may result in a unique polarization signal stemming from a galaxy. However, a majority of the previous studies have had limited frequency coverage and could not distinguish between the models. Narrow bandwidths greatly reduce the resolution in Faraday depth space, while broad channel widths decrease the maximum observable Faraday depth. Continuous sampling over a large frequency range allows for the recovery of the true polarization signal.

However, the development of broad observing bandwidths in recent years has the potential to decipher contributions from individual magneto-ionic structures along the line of sight. The Compact Array Broad-band Backend (CABB; Wilson et al. 2011) on the Australia Telescope Compact Array (ATCA) has opened up the a continuous frequency ranges of 1100–3100 and 4500–6500 MHz, sampled at 1 MHz intervals. With these wide bandwidths and high spatial resolution, we are able to evaluate and model the polarization properties of the radio emission on a pixel-by-pixel basis, investigate the origin of the polarized signal and attempt to answer whether the rotation we observe is a consequence of magnetic fields adjacent to or within the radio galaxy.

Motivated by the recent improvement in continuous frequency coverage, we observe NGC 612 (PKS B0131-367) in an attempt to conclusively determine the physical properties of all Faraday rotating components that contributes to the observed polarization. NGC 612 has been studied at multiple wavelengths and is an ideal candidate with which to carry these polarization studies. Due to its relatively low redshift ($z = 0.0297$, de Vaucouleurs et al. 1991), the two, large-scale lobes (Ekers et al. 1978) span a relatively large angular scale (∼18 arcsec) and is well-resolved by the ATCA.

Resolving NGC 612 is particularly interesting due to the marked difference in morphology between the two radio lobes. NGC 612 has been classified as having a hybrid radio source morphology (Gopal-Krishna & Wiita 2000) with the eastern lobe exhibiting strong FR-II (Fanaroff & Riley 1974) characteristics, marked by a hotspot ('HS', RA(J2000) = 01:34:17, Dec. (J2000) = −36:30:39), whereas the western lobe more closely matches an FR-I classification with a visible jet. The total radio power of NGC 612 is $P_{4.8\,\mathrm{GHz}} \sim 0.8 \times 10^{25}$ W Hz^{-1} (Morganti, Killeen & Tadhunter 1993), which falls between typical FR-I and FR-II values (Owen & Laing 1989; Owen & White 1991).

NGC 612 is a member of a galaxy group with seven members (Ramella et al. 2002) in which there is evidence of a recent interaction. This is supported by existence of the dust lane in the optical counterpart (Ekers et al. 1978; Kotanyi & Ekers 1979) in addition to a tenuous H I bridge reaching 400 kpc from the disc of NGC 612 towards its nearest neighbour, NGC 619 (Emonts et al. 2008). Furthermore, Tadhunter et al. (1993) argue that recent star formation has taken place, as suggested by the observation of strong and narrow absorption features in the optical spectrum, with weak [O II] and [O III] emission, and both Raimann et al. (2005) and Holt et al. (2007) observe a young stellar population throughout the stellar disc.

There is diffuse, soft (0.7–3 keV) X-ray emission associated with the lobes of NGC 612, with extended emission in the direction of the eastern lobe, described in Tashiro, Makishima & Kaneda (2000), who argue that the emission is likely due to the cosmic microwave background up-scattering off the synchrotron-emitting electrons in the lobes. Making basic assumptions of the geometry and distribution of matter within the lobes, Tashiro et al. (2000) use the observed quantities of spectral index in both the radio and infrared regimes, as well as the surface brightness of the radio continuum and X-ray emission, to estimate an implied magnetic field strength of the lobes of 1.6 ± 1.3 μG.

NGC 612 was selected as part of a larger sample of large angular-scale, Southern hemisphere radio galaxies, with each radio galaxy representing different intrinsic characteristics, radio morphology classifications, and environments. Future work will investigate the relationship between these various radio galaxy characteristics and the observed polarization properties. Work carried out in this paper is complimentary to recent work by Banfield et al. (2017), who use spectro-polarimetric observations of NGC 612 and its surrounding environment to motivate environmental impacts on radio morphology.

In this paper, we present a detailed study of the polarization properties of the radio galaxy NGC 612. The paper is structured as follows: we begin by describing the observations and data reduction are described in detail in Section 2, followed by a description of how the polarized signal was recovered from the data (Section 3). In Section 4, we introduce the different depolarization mechanisms and how we built and tested models of polarized emission using maximum likelihood and Markov chain Monte Carlo (MCMC) techniques. Our results are presented in Section 5, which describes the relative success of polarization models, in addition to introducing the parameter maps created from the best-fitting polarization solutions. The discussion (Section 6) focuses on differentiating between the different depolarization models and attempts to answer the question of the origin of the observed Faraday rotation signal. Our conclusions are presented in Section 7.

2 OBSERVATIONS AND DATA REDUCTION

All observations for this project were taken with the ATCA CABB (Wilson et al. 2011), which offers 2 GHz of continuous bandwidth and a spectral resolution of 1 MHz. The wide bandwidths of CABB are ideal for recovering accurate Faraday depths from multiple contributors within the synthesized beam – a wider range of observed wavelengths lead to better the resolving power in Faraday space (Brentjens & de Bruyn 2005).

NGC 612 was observed in multiple array configurations spanning a baseline range of 107–2923 m. Combining multiple array configurations allows for better sampling of the *uv*-plane leading to improved sampling of the galaxy on all angular scales. Our effective *uv*-coverage is shown in Fig. 1 for both the observing bands covering all observing days. A summary of the observations is given in Table 1, which lists the array configuration, total time on source and date of observation.[1] The mosaic pointings were Nyquist sampled at the resolution of the highest frequency channel (3100 and 6500 MHz). Each mosaic pointing was observed at 30 s intervals, switching to the phase and leakage calibrator PKS B0153-410 once numerous mosaic cycles completed. The time between observations of the phase calibrator was no more than 20 min.

The data were reduced, calibrated, and flagged using the MIRIAD software package (Sault, Teuben & Wright 1995). PKS B1934-638 was observed once per day as the absolute flux and bandpass calibrator. The bandpass, gains, and polarization solutions were calculated

[1] PKS B1934-638 is known to be unpolarized to less than the 0.2 per cent level. This is standard practice, as outlined in the MIRIAD user's guide (Sault et al. 1995).

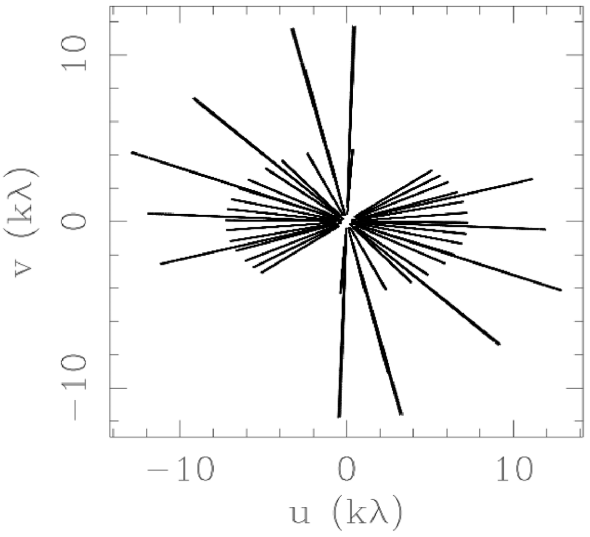

(a) 2100 MHz

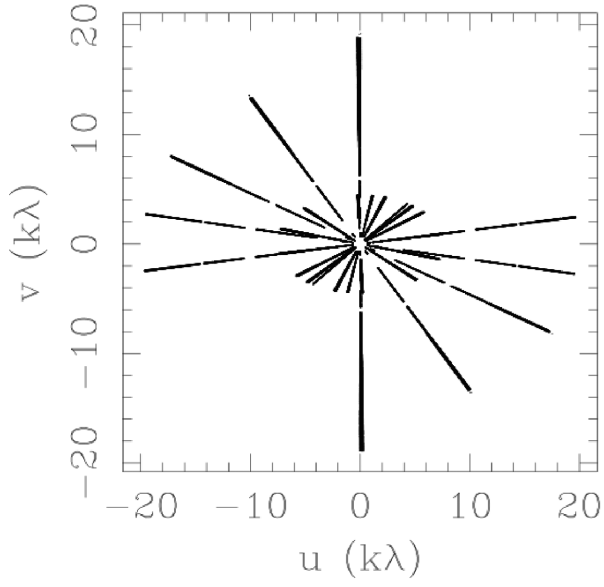

(b) 5500 MHz

Figure 1. Final *uv*-coverage for our observations of NGC 612 for observing bands centred at 2100 MHz (top) and 5500 MHz (bottom). As the bright galaxy was observed in short snapshots, there are negligible azimuthal tracks.

Table 1. Summary of the observing log for NGC 612, which is a subset of ATCA project C2776. Column 1 gives the array configuration; column 2 the central observing frequency in GHz. The total time spent on-source each run is listed in column 3. Column 4 gives the UT date of the commencement of the observations.

Array configuration	Observing frequency (MHz)	Time on-source (hours)	Observation date
1.5 C	2100	0.26	2012 Dec 03
1.5 C	5500	0.29	2012 Dec 03
EW 352	5500	0.77	2013 Jan 09
EW 352	5500	1.37	2013 Jan 10
750 C	2100	0.98	2013 Jan 25
750 C	5500	0.49	2013 Jan 26
6A	2100	0.1	2013 Feb 24

every 128 MHz in order to avoid any frequency-dependent calibrations. Sault & Cornwell (1999) showed that in order to carry out polarization calibration using an east–west array, for a source with unknown polarization levels, observations must be made at ≥3 parallactic angles. For observations made for this study, leakage calibration was carried out using the phase calibrator source, PKS B0153-410, as observations of this target mostly resulted in sufficient parallactic angle coverage. For short observations, where multiple observations of a point source resulted in inadequate parallactic angle coverage (e.g. 2013 February 24), the bandpass calibrator source PKS B1934-638 has been used to calculate leakage solutions.[2]

The data were flagged largely with the automated task PGFLAG, with minor manual flagging being carried out with tasks BLFLAG and UVFLAG. In total, 37 per cent and 19 per cent of the data were flagged in the 2100 and 5500 MHz bands due to radio frequency interference, respectively.

Naturally weighted Stokes *I*, *Q*, and *U* mosaic maps were made every 16 MHz. To avoid any resolution effects between frequencies, the dirty images were convolved to a common resolution of 1 arcmin. We drop the lowest frequency maps due to insufficient *uv*-coverage after flagging.

Joint maximum entropy deconvolution was performed on the mosaics with the task PMOSMEM. Using previously published values for the total flux density of NGC 612, we find a spectral index value of $\alpha = -0.65$ ($S \propto \nu^{\alpha}$). In the absence of single dish observations for an absolute flux reference, we estimate the expected total source flux extrapolating from this spectral index value and previous measurements (Fig. 2). To test the validity of this assumption, we additionally cleaned the Stokes *I* maps with a *multiscale clean* approach with the *Common Astronomy Software Applications* (CASA). We find that corresponding frequency Stokes *I* maps are nearly identical, with negligible variations in both total flux and on a pixel-by-pixel basis compared to the rms noise.

Cleaned images were generated with the task RESTOR. Our synthesized beam is 1 arcmin across where one pixel corresponds to 10 arcsec in angular size. At the distance to the galaxy of 121.5 Mpc, one beam corresponds to a physical size of ∼35 kpc for $H_0 = 73.0\,\mathrm{km\,s^{-1}\,Mpc^{-1}}$.

3 OBSERVATIONAL RESULTS

3.1 Imaging results

Our data reduction resulted in 92 independent channel maps in Stokes *I*, *Q*, and *U*. Typical maps of total intensity (Stokes *I*) and both linear polarizations (Stokes *Q* and *U*) are shown every 512 MHz in Fig. 3. We see a signal with clear linearly polarized emission stemming from both lobes. Corresponding frequency maps of polarized intensity ($P = \sqrt{Q^2 + U^2}$) were created from the final Stokes maps. It is immediately evident that the polarization signal changes as a function of position across NGC 612 (Fig. 3).

[2] During the 2012 October and 2013 April observing semesters, there existed a large ripple running through the middle of the 5500 MHz observing band for all observations involving ATCA antenna CA01. The ripple only affected the *Y*-polarization and was highly time variant. Significant effort was made to correct the erroneous data so that we might include all baselines involving CA01; however, the attempts were ultimately unsuccessful and the high-frequency polarization data were dropped from our analysis.

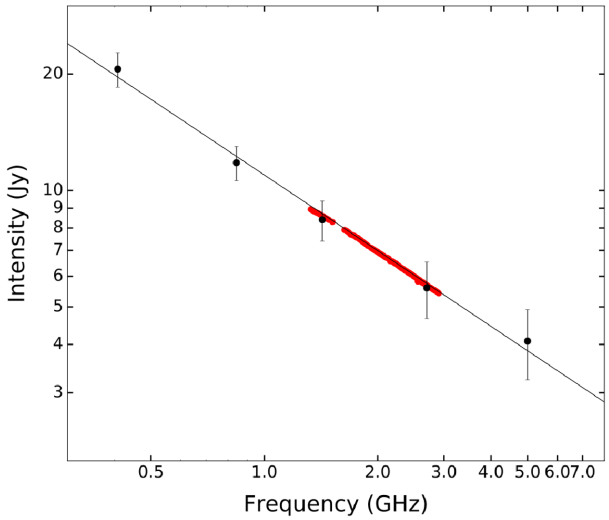

Figure 2. Measured flux density of NGC 612 as a function of wavelength. Our observations are shown in red with the displayed marker size of each measured flux being larger than the measured intensity errors. Measurements taken from previous literature are in black. Reference fluxes with corresponding errors are shown at 408 MHz (Schilizzi & McAdam 1975), 843 MHz (Mauch et al. 2003), 1.425 GHz (Fomalont 1968), 2.7 GHz (Bolton & Shimmins 1973), and 5.0 GHz (Wall & Schilizzi 1979). The figure is truncated and does not show a flux density value of 56 Jy at 85.5 MHz (Mills, Slee & Hill 1960). Updated flux density values at 408 MHz and 843 GHz were acquired through private communication with Dr. Richard Hunstead. A spectral index of $\alpha = -0.65$ is measured from our data.

Uncertainties in the intensity values of I, Q, U, and P were measured for each frequency interval by taking the rms value (σ) of an area in the final maps near, but not including, the radio emission. Pixels were masked if $>$ 10 per cent of the channels fell below a threshold of 8σ in Stokes I and 5σ in polarized intensity. We discard all edge pixels from the continuous, accepted pixels that comprise the radio galaxy. This results in 1277 usable pixels comprised of 45 independent beams for our analysis.

We also make a high-resolution, high-frequency total intensity map at 5500 MHz in order to trace the path of the jet associated with the lobes of NGC 612. The Stokes I imaging results are minimally effected by the hardware issues described in Section 2, leading the deconvolved map of Stokes I to be robust and giving us confidence in the jet position. Contours of the high-frequency position of the jet is marked by the cyan contours in Fig. 4 and as a grey dashed line in all subsequent parameter maps of the radio lobes.

3.2 Fractional polarization spectra

In order to decouple spectral effects from wavelength-dependent polarization, we adopt fractional polarized notation, such that $q = Q/I$, $u = U/I$, and $p^2 = q^2 + u^2$. We create fractional polarized spectra, by dividing the observed $Q(\lambda^2)$ and $U(\lambda^2)$ by a second-order polynomial model, bootstrapped to the Stokes I emission. We fit the Stokes I spectrum in linear $S(I)$ versus ν space to avoid overweighting higher frequency flux density measurements, thus leading to the creation of non-Gaussian noise when propagating the uncertainty as a function of frequency.

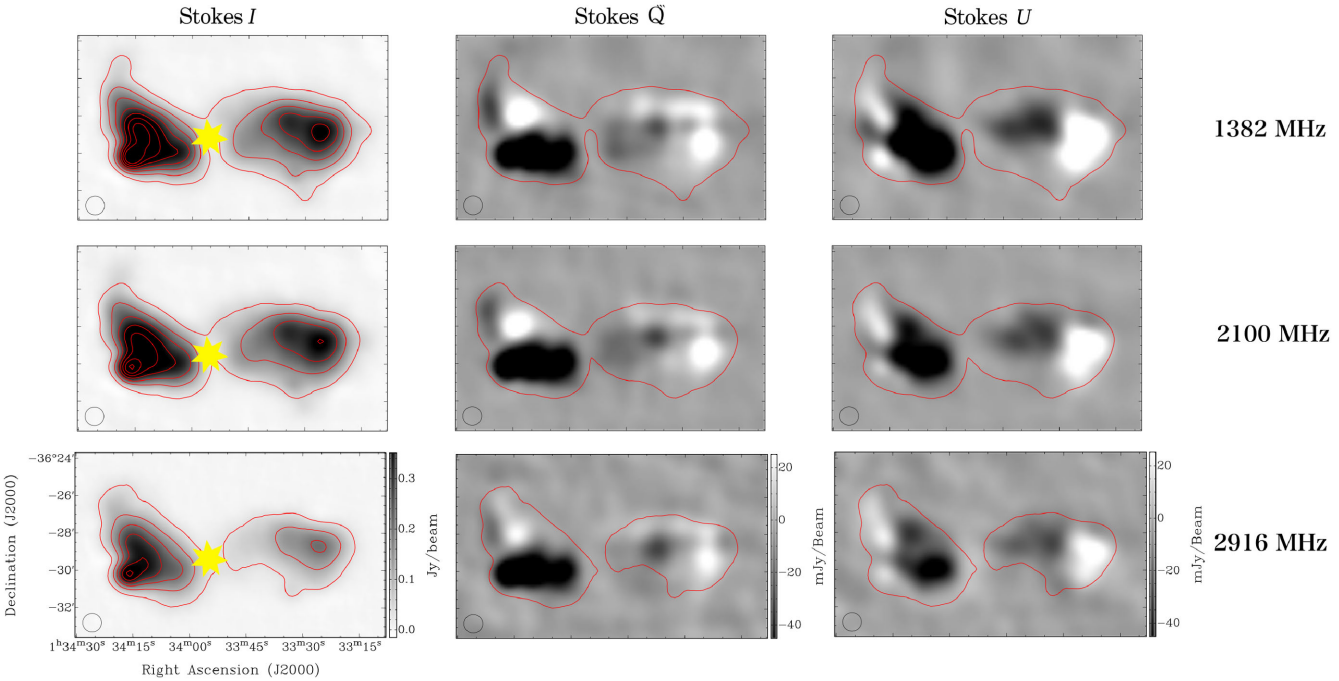

Figure 3. Maps of Stokes I, Q, and U (left, centre, and right, respectively) at wavelengths centred at 1332, 2100, and 2916 MHz in ascending order. These frequency channels represent the extremes and middle of the 2100 MHz observing band. Intensity levels are kept constant across the displayed frequency range with the colour bar shown in the bottom panel. The circular beam has a full width at half-maximum of 1 arcmin and is shown in the lower left-hand corner of each map. Stokes I contours are shown in red and represent total intensity values of 30–480 mJy beam^{-1} at intervals of 75 mJy beam^{-1} for the total intensity maps and the lowest intensity contour is shown on both the Stokes Q and U maps. The Stokes I rms noise levels are $\sigma_I =$ 5.4, 3.7 and 4.1 mJy beam^{-1} for 1382, 2100, and 2916 MHz, respectively. The rms noise levels of the Stokes Q and U maps are equivalent at each frequency with values of $\sigma_{Q,U} =$ 2.0, 1.5, and 1.9 mJy beam^{-1} for 1382, 2100, and 2916 MHz. The location of the optical galaxy is marked with a yellow star in all total intensity figures.

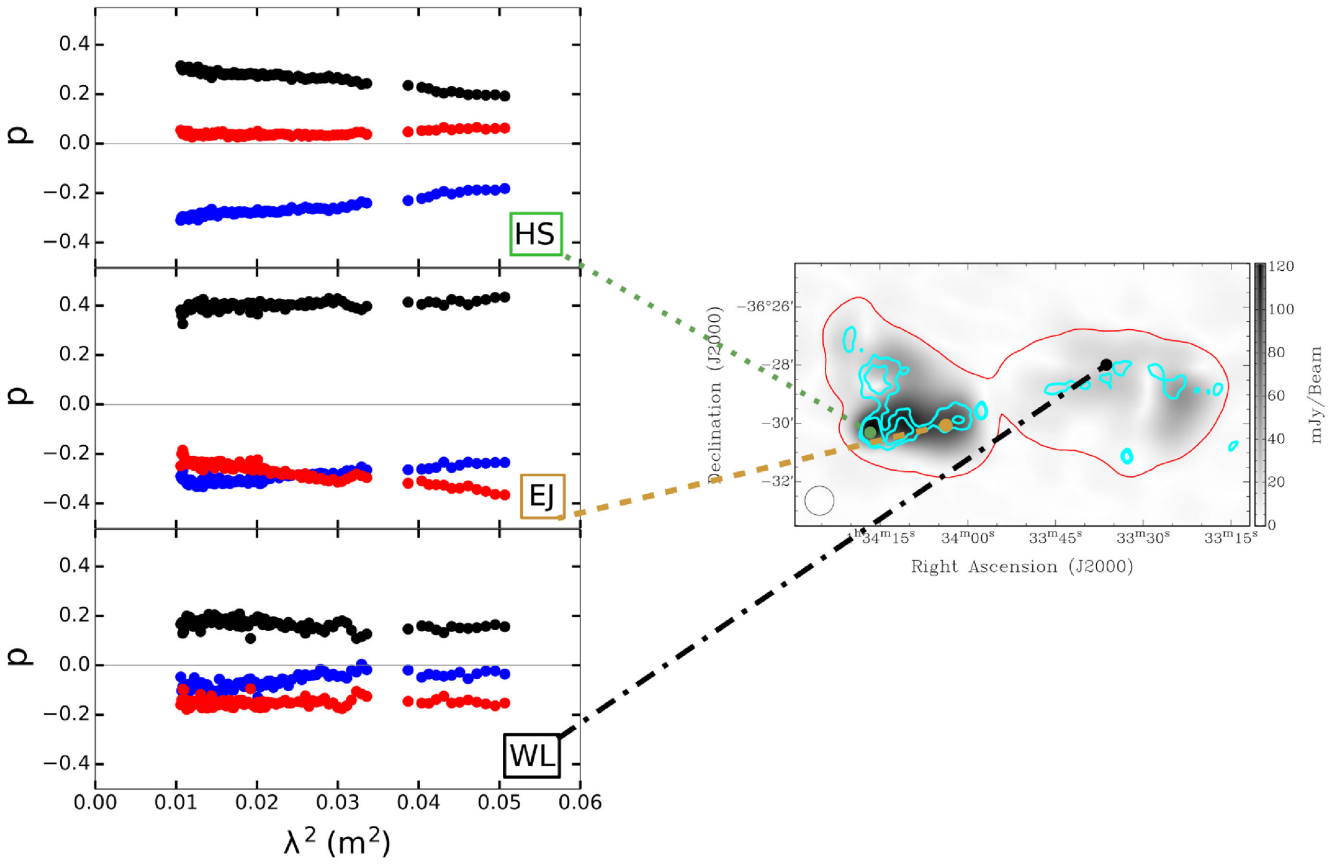

Figure 4. Polarized intensity map at 2100 MHz (right) with red contours outlining 30 mJy beam^{-1} in total intensity (Stokes *I*). Fractional polarized spectra are shown for the indicated pixel locations. Polarized fraction, p (P/I), is shown in black, q (Q/I) in blue, and u (U/I) in red versus λ^2. All data points are displayed on a scale larger than their corresponding errors. Point 'HS' represents the location of the hotspot in total intensity, point 'EJ' (eastern jet) is near the location of the optical counterpart (identified in Fig. 3), and point 'WL' is a pixel in the western lobe. The path of the jet, as determined from high-frequency imaging, is shown in cyan contours.

Fig. 4 shows the fractional polarization spectra of a few representative pixels across the source and also demonstrates the varying levels of polarization seen in the galaxy. Depolarization is defined as a negative change in the observed degree of polarization as a function of λ^2 ($dp/d\lambda^2 < 0$). We observe this trend most clearly in the region of the hotspot ('HS'), where observed level of polarization decreases as a function of λ^2.

Assuming the lobes are composed of an optically thin synchrotron radiation source, we calculate the spectral index for each extracted pixel by fitting the Stokes *I* spectrum to a single, emission component in log-space. In making this assumption, we are also assuming that the dominant polarization component is also the dominant spectral component, and this may not necessarily be true in the case of the projected area of the jet where it is possible to have two significant spectral components. Fig. 5 shows a map of spectral index across the lobes of NGC 612. The dashed line traces the projected path of the jet through the lobes.

Our analysis (Section 5) will partially focus on the three representative pixels shown in Fig. 4. The hotspot, denoted 'HS', represents the area of bright continuum emission at the far east end of the eastern lobe. The eastern jet, denoted 'EJ', is a pixel that is near the optical galaxy and marks the position of peak polarization. This pixel is located within the jet that can be seen stretching across the eastern lobe. The pixel in the western lobe, denoted 'WL', is a representative pixel for the majority of this lobe, which has on average a lower degree of polarization than the eastern lobe.

4 MODEL FITTING

In highly energetic environments such as radio lobes, complex magnetic field, and thermal electron structures will give rise to multiple rotation and/or emitting sources along the line of sight and the observed polarization signal may experience depolarization. Depolarization may be a result of turbulent mixing of gas in the lobes, the emitting and rotating material being co-spatial, or the spatial resolution of the observations. The effects of depolarization tend to be strongest towards longer wavelengths and the mechanism responsible contains insight on the overall structure of the radio lobes.

The observation of depolarization in Fig. 3.2 at the location of the hotspot makes it immediately evident that it will be necessary to involve some polarization models that are more complex (i.e. not Faraday thin) in order to accurately describe at least some of the observed polarization. In order to analyse the nature of the polarization of NGC 612 and its surrounding area, we test various single-component polarization models, which we detail below.

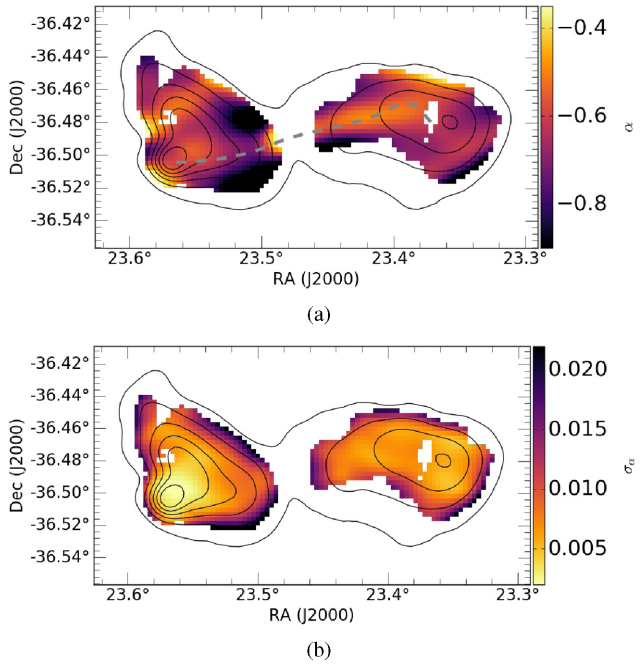

Figure 5. Spectral index values for each pixel evaluated as a single-component linear fit to the Stokes *I* spectrum in log-space (a) with corresponding 1σ uncertainty (b). In (a), the dashed grey line shows the path of the jet. Contours show the total intensity from 25 to 400 mJy beam^{-1} in intervals of 75 mJy beam^{-1}.

4.1 Polarization models

Polarized emission in the absence of a Faraday rotating medium can be expressed simply as

$$\mathcal{P} = p_0 e^{2i\Psi_0}, \tag{1}$$

where the p_0 is the intrinsic fractional polarization, Ψ_0 is the intrinsic polarization angle of the emission. If the polarized emission passes through a purely foreground, the polarization angle is rotated from its intrinsic value. This is the simplest scenario of Faraday rotation and the polarized signal that is observed can be expressed as

$$\mathcal{P} = p_0 e^{2i(\Psi_0 + \phi\,\lambda^2)}, \tag{2}$$

where ϕ is the Faraday depth at the distance of the magneto-ionized material. However, the observation of depolarization in Fig. 4 at the location of the hotspot makes it immediately evident that it will be necessary to involve more complex models in order to accurately describe at least some of the observed polarization.

There are typically three mechanisms that can lead to depolarization, all of which are presented with complete discussion in Sokoloff et al. (1998) and references therein, and all we briefly outline below.

4.1.1 *External Faraday dispersion (beam depolarization)*

If many turbulent polarizing cells are within the telescope beam – or if there is an ordered magnetic field that varies in strength and/or direction – the polarized emission will undergo different amounts of rotation along the different lines of sight. When the fluctuations are averaged across the entire beam area, the result is depolarization of the form

$$\mathcal{P} = p_0\, e^{2i(\Psi_0+\phi\lambda^2)}\, e^{-2\sigma_\phi^2\lambda^4}, \tag{3}$$

where σ_ϕ characterises changes in Faraday depth on scales smaller than our beam. This type of depolarization may occur when an expanding radio lobe sweeps up material from its surrounding environment. If this material is ionized or threaded by a homogeneous magnetic field, it would act as a thin Faraday screen, but would not depolarize the emission from the radio lobes (Bicknell, Cameron & Gingold 1990). Fluctuations in the magnetized intergalactic medium is the other, albeit more common, application of external Faraday dispersion (EFD) and has been used to study magnetic fields in galaxy groups and clusters (Laing et al. 2008).

Due to the purely external dependence of this type of depolarization, and its dependence on the observing beam, this type of depolarization is often referred to as *'beam depolarization'*.

4.1.2 *Differential Faraday rotation (depth depolarization)*

If the emitting and rotating medium are mixed in the presence of a regular magnetic field, the emission on the far side of the radio lobe will experience a different amount of rotation when compared to the emission at the near edge of the lobe. When summed over the line of sight, this will lead to depolarization that takes the form of

$$\mathcal{P} = p_0\, e^{2i\left(\Psi_0+\frac{1}{2}\,\phi\lambda^2\right)}\,\frac{\sin\,\phi\lambda^2}{\phi\lambda^2} \tag{4}$$

for a symmetric, uniform slab, where ϕ is the Faraday depth through the region. For an emitting and rotating medium of an arbitrary thickness, the classical RM is equal to $\frac{1}{2}\phi$, i.e. the actual Faraday depth is equal to twice the observed RM.

4.1.3 *Internal Faraday dispersion*

This scenario is similar to differential Faraday rotation (DFR), but rather than being concurrent solely with a uniform magnetic field, the emitting and rotating medium may also be in the presence of a turbulent magnetic field. Any emission now must undergo a random walk through the turbulent field, which results in the plane of polarization being rotated different amounts. For the simplest case, we consider a Gaussian distribution of Faraday depths within the lobes,

$$\mathcal{P} = p_0\, e^{2i\Psi_0}\,\frac{1 - e^{2i\phi\lambda^2 - 2\zeta^2\lambda^4}}{2\zeta^2\lambda^4 - 2i\phi\lambda^2}, \tag{5}$$

with a mean Faraday depth ϕ and standard deviation ζ. Internal Faraday dispersion (IFD) characterizes both the uniform and turbulent magnetic fields, with the behaviour becoming identical to that of DFR in the case of a dominating uniform field.

4.1.4 *Multicomponent emission*

There is also the possibility that there are multiple emitting, rotating, and/or depolarizing components along the line of sight. Multiple component models can be constructed by summing the complex polarization from individual models

$$\mathcal{P} = \mathcal{P}_1 + \mathcal{P}_2 + \mathcal{P}_3 + ... + \mathcal{P}_N. \tag{6}$$

A complex polarization signal can often have a beating pattern as a function of λ^2 as the rotation due to different components passes into and out of phase.

We limit our investigation to a single polarized component. Upon inspection, the higher order features of the *q* and *u* spectra are likely

contaminated by instrumental effects. This minimizes the possibility of overfitting the data. In any case, one component is sufficient to describe the bulk of the polarized signal. This limits the physical interpretation of the polarized morphology, but as we will demonstrate in the sections that follow, acceptable solutions can be found. We found that expanding the number of components to be greater than one can fit the data closely; however, the degeneracy between two-component models and their parameters prevents interpretation.

4.2 Modelling procedure

In order to test which mechanisms may be responsible for the observed polarization, the single-component depolarization models introduced in Section 4.1 (i.e. thin, EFD, DFR, and IFD) are explored individually. The extracted $q(\lambda^2)$ and $u(\lambda^2)$ data are simultaneously fit to each corresponding depolarization model using a maximum likelihood method. We employ the EMCEE PYTHON module (Foreman-Mackey et al. 2013) to fit the complex polarization parameters of each depolarization model. Unlike Levenburg–Marquardt fitting, MCMC has the added benefit of better exploration of parameter space, as well as returning numerically determined errors to model parameters. The log-likelihood of the complex polarization model of the joint q–u chi-squared (χ^2) is minimized to find the best-fitting parameters. For each pixel in our data set, we initialize a set of 250 parallel samplers that explore the n-dimensional parameters space (where n is the degrees of freedom). Each of these walkers iteratively calculate the likelihood of a given location in parameter space and in doing so map out a probability distribution for a set of parameters. For any given depolarization model, the possible parameter solutions were forced to be physical (i.e. $0 \leq p \leq 1$). In order to maximize the effectiveness of initial burn-in phase and have the walkers settle on a parameter space, each iteration of MCMC used the previous pixel's best-fitting values as an initial guess.

To assess the goodness of fit of each models, the reduced chi-squared value (χ^2) was recorded for each pixel. χ^2 is defined as

$$\chi_r^2 = \frac{1}{\nu} \sum_{i=1}^{n} \left(\frac{x_i - \mu_i}{\sigma_i} \right)^2, \quad (7)$$

where x_i is the ith independent data point with Gaussian noise, σ_i; μ_i is the model prediction and ν is the number of free parameters. This statistic penalizes according to how many standard deviations lie between the observed point and the model and generally serves as a means of assessing the success of a particular model fit to the observed data. However, it can be misleading to employ χ^2 when comparing the relative success between models, as it is possible to build, and fit, arbitrarily complex models.

In the case of Gaussian noise, the χ^2 is equivalent to $-2\log\mathcal{L}$. We note that χ^2 is not an ideal statistic with which to evaluate the success of these models as our sampling of λ^2-space is non-linear, which in turn overweights the importance of low-λ^2 samples and will downweight samples at high-λ^2. Additionally, for a sufficiently robust data set of a simple polarized spectrum, a returned $\chi^2 < 1$ is not uncommon. This is due to the minimum number of model parameters of any physical polarization model being 3 (p_0, Ψ_0, ϕ) and a model with fewer parameters is deemed unphysical. In these instances, we acknowledge the overfitted solution, but use the returned best-fitting parameters for our analysis.

5 MODELLING RESULTS

Fitting a single polarized component to NGC 612 returns a $\chi^2 \leq 1.5$ for more than 60 per cent of pixels (Fig. 6); expanding this to include all pixels with $\chi^2 \leq 2$ results in the acceptance of more than 90 per cent of pixels across the lobes of NGC 612. We therefore believe that one polarization component is sufficient to describe the bulk of the polarized signal. Upon inspection, any higher order features of the q and u spectra are likely contaminated by instrumental issues that affected the ATCA at the time of observation (e.g. 300 MHz spectral wiggle, Section 2). Therefore, we limit our investigation to a single polarized component. This minimizes the possibility of overfitting the data and overinterpreting the results. Although this limits the physical interpretation of the polarized morphology, we will demonstrate in the sections that follow that a favourable solution can be found by examining the physics of the implied model. In the following section, we explore the relative success of each model with the aim of determining which best represents the polarization signature associated with the radio galaxy.

Fig. 7 represents the best-fitting solutions to each of the polarization models for three single-pixel spectra. The pixels are selected to be representative of three independent regions of the radio lobes: the hotspot, the east jet, and the western lobe (see Fig. 4 for specific locations). Below each model fit, the residual polarization spectrum is shown to demonstrate any latent structure in the spectrum. The similarity between each model's best fit is immediately evident, with the largest discrepancy between model solutions occurring at the location of the hotspot (*top row*, Fig. 7). In this region, only polarization mechanisms with an explicit dispersion term (EFD, IFD) are able to fit the spectra at large λ^2.

Global χ_r^2 values for each polarization model are shown in Fig. 6. The χ_r^2 maps allow the reader to assess a model's overall success in fitting the polarization signal of the entire radio galaxy. Table 2 reports the mean reduced chi-squared ($\overline{\chi_r^2}$) for an area equivalent to the synthesized beam in three regions of the radio lobes. Given the relative similarity in model-fitting results, as shown in Fig. 7, it is unsurprising that each polarization model also returns a similar global success. In addition to the region of the hotspot, the western lobe has a marginal preference for dispersion models (see Table 2).

5.1 Parameter maps

In this section, we present the best-fitting parameter maps returned from our *qu*-fitting routine. The parameter values for each of the polarization models are similar enough to allow us to present the general signal trends here. Detailed parameter maps and their corresponding uncertainties for each individual polarization model as given in the Appendix.

5.1.1 *Intrinsic degree of polarization*

Fig. 8 shows the intrinsic polarization across the lobes of NGC 612. The polarization signal peaks nearest the location of the optical galaxy (shown as a yellow star in Fig. 3). There appears to be strong polarization along the path of the jet in the eastern lobe through to the hotspot, whereas the polarization in the western lobe peaks at the edge of the lobe furthest away from the optical counterpart. The grey dashed line shown in Fig. 8 traces the jet, as identified from high-frequency observations (Fig. 4).

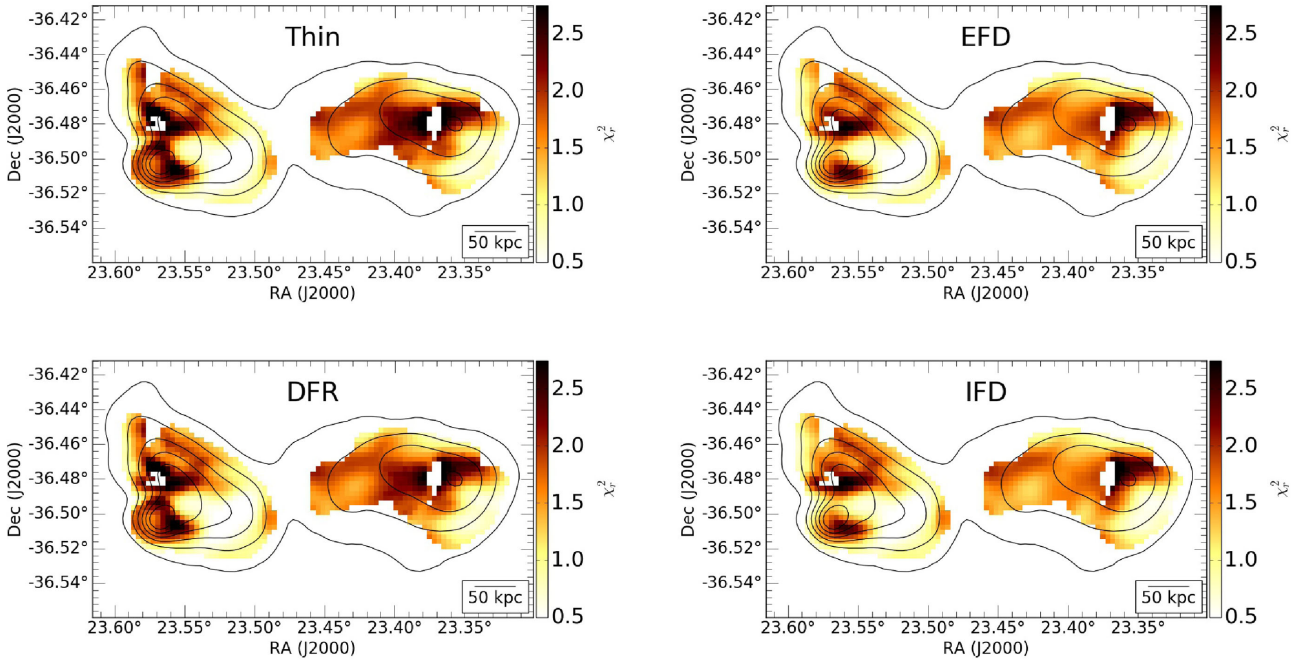

Figure 6. χ^2_r values at each imaged pixel for all polarization models discussed in this work. Black contours outline total intensity levels spanning 25–400 mJy beam^{-1} in 75 mJy beam^{-1} increments. A scale bar is shown in the bottom right-hand corner of each figure. All models have a tendency to have similar χ^2 values.

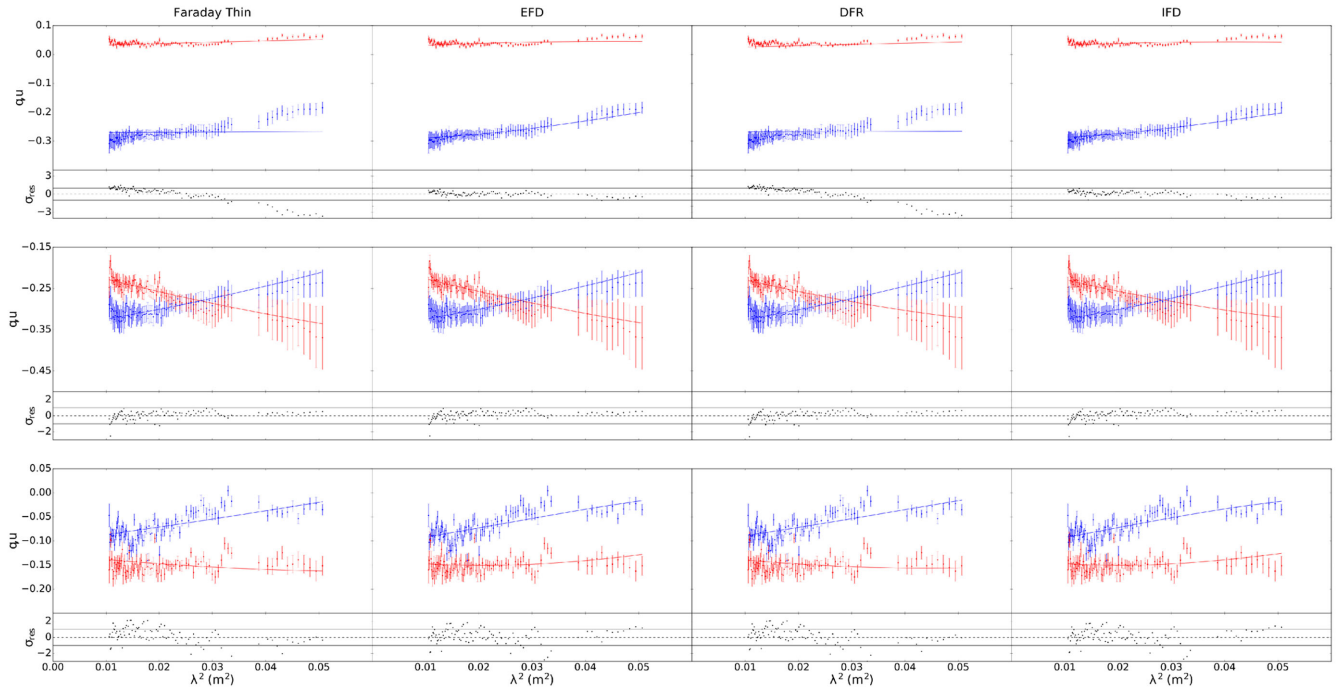

Figure 7. Grid of best-fitting results from *qu*-fitting to three distinct pixels in NGC 612. The columns represent the models tested, while each row represents the three pixels tested. Each pixel was chosen from a unique region in the radio lobes – the hotspot (top), the eastern jet (middle), and western lobe (bottom). The blue and red points are the measured q and u data, respectively. The blue and red lines are the resulting joint best-fits from *qu*-fitting. The bottom panels of each cell show the residual degree of polarization ($(p_{obs} - p_{mod})/\sigma_p$) for each model, with the solid black lines indicating +1 and $-1\sigma_p$ deviations from the observations.

5.1.2 Intrinsic polarization angle

Fig. 9 presents the intrinsic polarization angle of the electric field vector (Ψ_0). The orientation of the plane-of-the-sky magnetic field ($B_\perp$) is orthogonal to the position angle of the electric vector. The length of each vector in Fig. 9 is representative of the relative degree of polarization, with the longest vector equivalent to 40 per cent polarization. We see coherence in the direction of

Table 2. Mean χ_r^2 for each depolarization models discussed in Section 4 for the locations shown in Fig. 4. The mean is calculated for a number of pixels equivalent to our synthesized beam.

Pixel location	Thin	EFD	DFR	IFD
Hot spot	1.9	1.7	1.9	1.7
Eastern jet	0.40	0.40	0.42	0.43
Western lobe	2.0	1.6	1.9	1.6

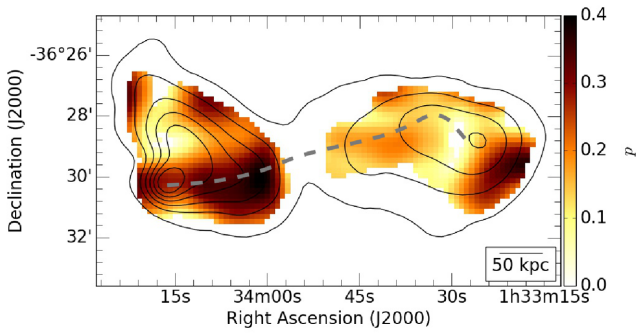

Figure 8. Map of the intrinsic polarization fraction in the radio lobes. All polarization models yield similar intrinsic polarization maps. The grey dashed line traces the peak in polarized intensity, which we believe to be representative of the path of the jet. Black contours outline total intensity levels spanning 25–400 mJy beam^{-1} in 75 mJy beam^{-1} increments.

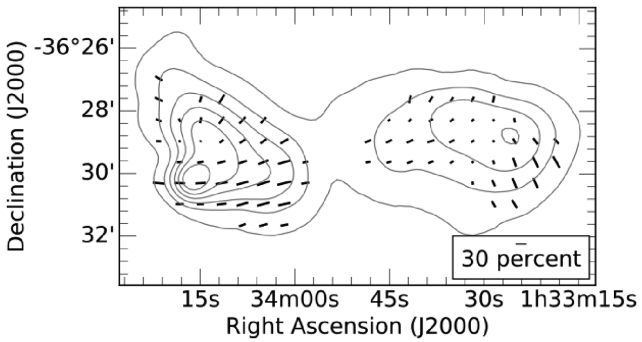

Figure 9. Map of the intrinsic polarization angle (Ψ_0) towards NGC 612. The length of each vector is proportional to the polarized intensity, with a representative fraction represented in the bottom left corner. Black contours outline total intensity levels spanning 25–400 mJy beam^{-1} in 75 mJy beam^{-1} increments.

the intrinsic polarization angle on scales larger than the scale of our synthesized beam. In both the eastern and western lobes, the direction of the polarization angle nearest the optical counterpart appears to be nearly parallel to the direction of jet launch, while X-ray observations have found to be nearly perpendicular to our line of sight (Eguchi et al. 2011).

5.1.3 *Faraday depth*

Maps of Faraday depth are shown in Fig. 10. The signal is nearly homogeneous across the source and varies on scales that are generally many times larger than our 1 arcminute beam. The dominant Faraday depth signal across the radio lobes of NGC 612 is positive, implying that the magnetic field along the line of sight is oriented

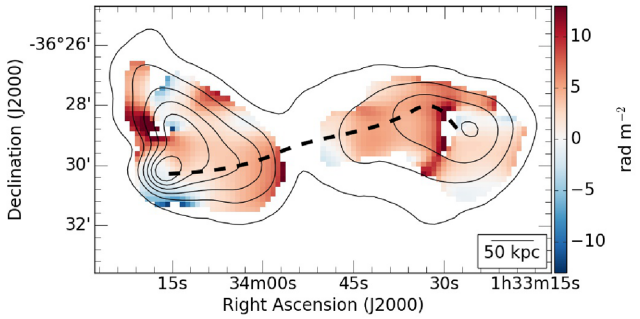

Figure 10. Faraday depth across NGC 612, as returned from the EFD model. The grey dashed line traces the path of the jet. DFR and IFD models show a similar trend but return ϕ-values that are a factor of 2 larger in magnitude per pixel. Black contours outline total intensity levels spanning 25–400 mJy beam^{-1} in 75 mJy beam^{-1} increments.

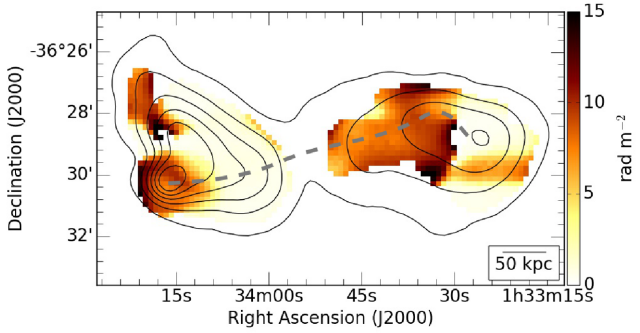

Figure 11. Map of Faraday dispersion (σ_ϕ) returned from *qu*-fitting. Best-fitting values of internal Faraday dispersion (ζ) are double that of the EFD. Black contours outline total intensity levels spanning 25–400 mJy in 75 mJy increments. The grey dashed line traces the path of the jet, as identified in higher frequency observations.

predominantly towards the observer. The only considerable exceptions to this orientation is surrounding the location of the hotspot in the eastern lobe, where the Faraday depth sign is predominantly negative.

DFR and IFD models return a similar trend to that seen in Fig. 10, but ϕ-values are a factor of 2 larger per pixel. As we have discussed in Section 4.1, this is an expected result. The mean Faraday depth for the Faraday simple components (thin and EFD) are $\overline{\phi}_s = +3.3 \pm 3.5$ rad m^{-2}. The mean Faraday depth of the complex models (DFR and IFD) is $\overline{\phi}_c = +6.8 \pm 6.7$ rad m^{-2}. Previous Faraday rotation studies of the lobes of NGC 612 have found a simple Faraday depth that is in agreement with both $\overline{\phi}$ estimates ($+7 \pm 5$ rad m^{-2}, Haves 1975; $+6 \pm 1$ rad m^{-2}, Simard-Normandin, Kronberg & Button 1981).

5.1.4 *Faraday dispersion/depolarization*

Fig. 11 shows values of EFD (σ_ϕ) for all pixels across the radio lobes. By contrast, the internal Faraday dispersion (ζ) values returned are twice the magnitude of those in Fig. 11. Assuming that depolarization scales with dispersion levels, we see varying level of depolarization as a function of position on the lobes of NGC 612.

Comparing similar χ_r^2 values from Fig. 6, we see that although models with dispersion terms (e.g. EFD and IFD) yield non-trivial dispersion values, there is often minimal improvement to the χ_r^2

when compared to models without a depolarization term (e.g. thin and DFR). This is especially true in the west lobe. We therefore argue that not all regions of NGC 612 require a dispersion model (EFD and IFD). Indeed the strongest dispersion values are located in areas of the lobes that are best fit with a depolarization term, in that the returned χ^2 is lower. In the region surrounding the hotspot, there are considerable amounts of Faraday dispersion, which increases in magnitude until it peaks at the edge of our pixel sample.

6 DISCUSSION

It is not possible to definitively determine which polarization mechanism is responsible for the observed Faraday rotation towards NGC 612 using the χ^2_r statistic alone. The close χ^2_r values in Table 2 and Fig. 6 show that all single-component models are capable of explaining the observed polarized signal at similar confidence levels. In the following subsections, we consider the physics of the observed Faraday depth signal in conjunction with the relative location of the thermal material along the line of sight. We apply any additional information available that may be able to help in distinguishing between models. The key difference in the interpretation of the polarization models is the location of the Faraday rotating material. The Faraday simple models (thin and EFD) have the rotating material external to the synchrotron radio lobes, whereas the Faraday rotation of the complex polarization models (DFR and IFD) is taking place within the radio lobe. For the remainder of the discussion, we refer to the Faraday simple models as 'Ext' and the complex models as 'Int', symbolising where the Faraday rotation is taking place.

6.1 Minimum energy estimates

We can estimate the minimum energy magnetic field needed to sustain the lobes of NGC 612 using equation (4) from Beck & Krause (2005). We break the lobes into two symmetric rectangular slabs each with a line-of-sight path-length of 140 kpc, and spectral index of $\alpha = -0.65$. At 2100 MHz, the eastern lobe has a surface brightness of 144 mJy beam^{-1} and an average polarized fraction of 23 per cent. The western lobe has a surface brightness of 121 mJy beam^{-1} and an average degree of polarization of 16 per cent. We assume that the polarized emission comes from a regular field with all possible inclinations and that the synchrotron plasma has a filling factor (f) of 0.1 throughout the lobes. We have no information on the proton-to-electron ratio ($\boldsymbol{K}_0$); therefore, we assume unity. With these estimates in mind, we find minimum energy magnetic field strengths of 4.3 and 4.2 μG for the eastern and western lobes, respectively. These estimates, in turn, lead to energy densities of 2.0×10^{-13} and 1.8×10^{-13} erg cm^{-3} for the eastern and western lobes, respectively. The field strength is not highly dependent on the inclination of the magnetic field under the assumption that the angle is averaged over the entire synchrotron volume of the lobes. On the other hand, we note that these estimates depend strongly on the filling factor (f) and the $\boldsymbol{K}_0$ value.

Our average minimum energy estimate of $\overline{B} \sim 4.2$ μG is not within the range provided by Tashiro et al. (2000), who use diffuse X-ray emission and find an implied field strength of $B \simeq 1.6 \pm 1.3$ μG for both lobes. Exploring the possibility that the variation between values could be a result of our estimation of effective path-length and $\boldsymbol{K}_0$, we evaluate the minimum-energy magnetic field for decreasing f and increasing $\boldsymbol{K}_0$. Each iteration results in a larger estimation of the implied magnetic field strength and we are unable to mediate the discrepancies between our estimate of $\overline{B}$ and that reported by Tashiro et al. (2000) with this method. We note that equipartition field strengths can be overestimates of the true magnetic field strength by up to a factor of 3 (Croston et al. 2005). If our measurement of the magnetic field is indeed an overestimate, a correction factor of 0.3 reconciles the differences between our $\overline{B}$ and that of Tashiro et al. (2000).

6.2 External versus internal Faraday rotation

6.2.1 *The Milky Way foreground*

One possibility is that the observed Faraday rotation is dominated by a local Galactic component. At a Galactic latitude of −77°, the Galactic contribution has been estimated to be on the order of a few rad m^{-2} (Oppermann et al. 2015). The magnitude of this Galactic Faraday depth estimate is of the same order as the observed Faraday depth across the radio lobes ($\overline{\phi}_{\rm ext} = 3.3$ rad m^{-2}; $\overline{\phi}_{\rm int} = 6.5$ rad m^{-2}). Therefore, it is necessary to further investigate and characterize the Faraday contribution from the Milky Way.

Stil, Taylor & Sunstrum (2011) show that the Faraday depth of the Milky Way is coherent on angular scales of a few degrees. NGC 612 has an angular scale of ∼18 arcmin across the two radio lobes, suggesting that there would be minimal variation in the projected Faraday depth on the radio galaxy. However, Fig. 10 shows multiple regions on NGC 612 where the intensity of the Faraday depth change over scales of a few arcminutes.

Many of the areas where the Faraday depth is seen to change correspond to regions of interest that are local to NGC 612. Fig. 10 shows that in the eastern lobe, the magnitude of the Faraday depth decreases as a function of distance from the optical counterpart. In the western lobe, the Faraday depth is seen to increase in magnitude leading up to a ridge of depolarization, first seen in Fig. 4. The most convincing trend in the Faraday depth is in the region of the hotspot, where the sign of the Faraday depth is observed to change. We will discuss the specific location of the hotspot in more detail in a subsequent section (Section 6.4), but the morphological correlation between ϕ and Stokes I strongly suggest that the bulk of the observed Faraday rotation is taking place within or near the lobes of NGC 612. It follows that while the Galaxy is responsible for some amount of Faraday depth, it is unlikely that it is responsible for the bulk of the observed Faraday rotation.

6.2.2 *The ambient X-ray IGrM*

Guidetti et al. (2011, 2012) have argued that the Faraday rotation associated with radio lobes is due to the radio galaxy being embedded in a halo of thermal material. In these instances, the galaxies investigated are members of galaxy clusters and the radio lobes were thought to be embedded in a halo of hot X-ray gas. The galaxy group environment often lacks a diffuse X-ray component; however, Tashiro et al. (2000) observe excess diffuse, soft X-ray emission extending ∼200 kpc away from NGC 612, and argue the X-rays have been emitted via the IC process, signifying the presence of free electrons in the intragroup medium.

If we assume that the diffuse material in which NGC 612 is embedded is threaded with a coherent magnetic field, then naïvely, any change in the distribution of the X-ray-emitting gas would correlate with a change in the observed Faraday rotation. This assumption of the foreground magnetic field also implies that any regions that are devoid of X-ray-emitting gas will correspond with a Faraday depth signal that is consistent with zero. Tashiro et al. (2000) point out a clear anisotropy in the soft X-ray intensity with the majority of

emission being associated with the eastern lobe. By contrast, the observed Faraday depth signal is largely isotropic across the two lobes. If the radio galaxy were embedded in a volume of hot gas, the apparent uniformity of the Faraday depth signal becomes difficult to explain given the lopsided nature of the X-ray emission. While this discrepancy does not serve as direct evidence against Faraday rotation due to a magnetized intragroup medium, it does raise some intriguing concerns as to what is responsible for the observed rotation. Additional high-resolution X-ray imaging of the hot gas on the scale of the lobes is needed for further analysis of the potential for external Faraday rotation due to the immediate environment.

6.2.3 *A swept-up thin skin*

It is also possible that the expanding lobes of NGC 612 have swept up and compressed the surrounding intragroup medium, as has been argued to be the case by Rudnick & Blundell (2003), although limitations in their specific approach are detailed in Ensslin et al. (2003). In this scenario, the observed Faraday depth signal is due to the synchrotron lobes being girt by a thin skin of thermal material.

We explore this possibility by assuming such a boundary layer has a depth $\mathrm{d}l \sim 20$ kpc; which is approximately one-tenth of the scale height of the lobes. In Section 6.1, we estimate the average total magnetic field in the lobes of NGC 612 to be $\overline{B} \sim 4.2\,\mu$G. As we have no knowledge of the relative field strengths of the line-of-sight component, we assume a geometrical upper limit of $B_{\parallel} \sim B/\sqrt{3} \sim 2.4\,\mu$G. Using a mean Faraday depth of $\overline{\phi}_{\mathrm{EFD}} = +3.3\,\mathrm{rad\,m^{-2}}$, we derive an implied electron density for a thin skin of $n_e \simeq 8 \times 10^{-5}\,\mathrm{cm^{-3}}\,(\phi/3.3\,\mathrm{rad\,m^{-2}})\,(B_{\parallel}/2.4\,\mu\mathrm{G})\,(\mathrm{d}l/20\,\mathrm{kpc})$.

By comparison, O'Sullivan et al. (2013) find an implied density of $n_e \sim 1.5 \times 10^{-3}\,\mathrm{cm^{-3}}$ for the lobes of Centaurus A, assuming the same skin depth ($\mathrm{d}l \sim 20$ kpc). They argue that the compression of material in the intragroup medium alone is not able to account for such a high density. By contrast, our estimate of the electron density of a thin-skin Faraday screen is a factor of 10 less. An intragroup medium equivalent to our required density is typical of many galaxy groups (Mulchaey & Zabludoff 1998; Sun 2012) and accumulating a population of ionized material of this density from the surrounding medium seems plausible, given a moderate ionization fraction as insinuated by the surrounding X-ray IGrM. Many theoretical models of the evolution of radio lobes assume that the surrounding medium has zero magnetization (e.g. Gourgouliatos, Braithwaite & Lyutikov 2010) and typical observed magnetization levels in an intragroup medium have been quite low at a radius of hundreds of kiloparsec from a galaxy group centre. However, Tashiro et al. (2000) argue that the magnetic energy density of the diffuse, large-scale X-ray plasma is roughly equal to the electron energy density of the lobes of NGC 612. In order to accumulate a density of a thin skin of $n_e \sim 8 \times 10^{-5}\,\mathrm{cm^{-3}}$, little compression of X-ray plasma is required.

We note that our assumed thin-skin path-length is largely speculative and motivated by similar values used for other radio lobes and the derived n_e used in the previous argument is inversely proportional to the path-length of the thin skin. To explore how this may change our argument of the thin-skin approximation, changing the path-length by a factor of 2 (i.e. $10\,\mathrm{kpc} \lesssim \mathrm{d}l \lesssim 40\,\mathrm{kpc}$) results in an implied electron density within the range of $2 \times 10^{-4}\,\mathrm{cm^{-3}} \lesssim n_e \lesssim 4 \times 10^{-5}\,\mathrm{cm^{-3}}$. This range of electron densities would still be physically achievable through the compression of the X-ray IGrM.

Given the lopsided distribution of X-ray plasma, the apparent uniformity of the Faraday depth signal in NGC 612 might be explained if the expanding lobes have swept up the ambient IGrM as they expand outward. Hydrodynamic simulations carried out by Bicknell et al. (1990) show that as lobes expand, it is possible for Kelvin–Helmholtz instabilities to form on the surface of the lobe due to feedback between the synchrotron material and the surrounding medium. In such a case, waves of material would appear on the surface of the radio galaxy, resulting in a unique Faraday depth pattern. Bicknell et al. (1990) also point out that a positive and negative variation in the sign of the Faraday depth should exist on a scale length equivalent to half-wavelength of the eddy. Anderson et al. (2017) have also studied such Faraday rotation signals for the lobes of Fornax A. We adapt a similar approach in exploring the possibility that the eddies can be physical structures below.

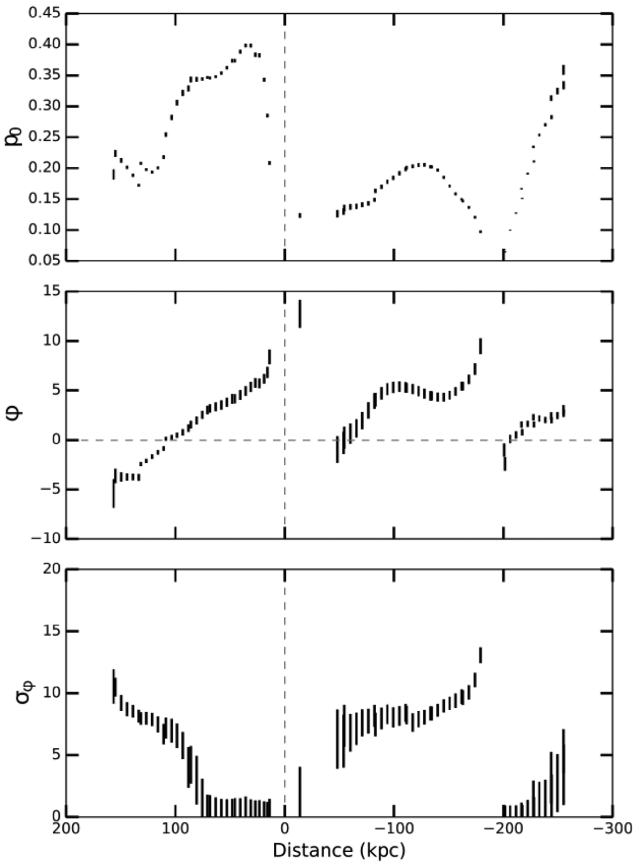

Figure 12. Intrinsic polarization, Faraday depth and Faraday dispersion as a function of position along the lobes of NGC 612, as traced by our assumed jet path (e.g. Fig. 8). The length of each tick mark represents the corresponding uncertainty at each position. The x-axis is indicative of the distance from the optical galaxy, with negative values indicating positions west of the galaxy. The vertical dashed line therefore marks the position of the host galaxy. The horizontal dashed line in the middle plot indicates $\overline{\phi} = 0\,\mathrm{rad\,m^{-2}}$.

Assuming that the jet is the dominant driving force for the expansion of the radio lobes, we choose to evaluate the polarization properties along the path that the jet traces, as shown in Fig. 10. The middle panel of Fig. 12 shows a rough sinusoid in the Faraday depth values as a function of distance from the optical counterpart. The half-wavelength of the surface wave appears to be $(\lambda/2) \sim 1.1$ arcmin ~ 40 kpc. Although in all instances we do not see the Faraday depth change when the gradient of the Faraday depth changes direction, which is expected from Faraday eddies, we note that we have not corrected for the Faraday rotation contribution

from the Milky Way, which may be shifting the observed Faraday depth to more positive values.

If we assume that the depth of the surface wave (d_e) is related to the wavelength of the eddy (λ_e), by a ratio of $d_e/\lambda_e \sim 0.3$ (Bicknell et al. 1990) it is possible to estimate n_e and d_e using equation (5.2) from Bicknell et al. (1990),

$$\Delta\phi \sim 0.49 \times n_e B_\parallel \lambda_e, \tag{8}$$

where $\Delta\phi$ is the change in Faraday depth between peaks. From Fig. 12, we can see that the peak-to-peak difference in Faraday depth is $\Delta\phi \simeq 6\,\mathrm{rad\,m^{-2}}$. Using our previously discussed estimate of $B_\parallel \simeq 2.4\,\mu\mathrm{G}$ and an eddy wavelength of $\lambda_e \sim 80\,\mathrm{kpc}$ (centre plot, Fig. 12), we find that the necessary electron density in the surface wave would be $n_e \simeq 6 \times 10^{-5}\,\mathrm{cm^{-3}}$ with an implied surface wave depth of $d_e \simeq 20\,\mathrm{kpc}$.

This is in excellent agreement with our thin skin estimate using the mean Faraday depth, although there are large uncertainties in our assumptions. This exercise argues that the observed Faraday signal associated with the bulk of the lobes of NGC 612 can be explained by Faraday eddies formed via an interaction with the X-ray IGrM. This scenario also indicates a preference for the Faraday rotating material to be located external to the synchrotron-emitting plasma.

6.3 Internal Faraday rotation

In contrast to the previous section, we now explore the possibility that the thermal- and synchrotron plasmas are located co-spatially within the radio lobes.

NGC 612 contains a young stellar population with on-going large-scale star-formation throughout the disc of the galaxy (Emonts et al. 2008). It is possible that as the lobes of NGC 612 expanded through the disc of the optical galaxy, it advected some material from the stellar disc (Begelman & Cioffi 1989; Churazov et al. 2001).

The advection process may be responsible for the observed Faraday rotation, since any thermal material in the lobes would have been entrained from the galactic disc (Laing & Bridle 2002). In this instance, the synchrotron emitting plasma is mixed with the thermal material from the galaxy and the bulk of the observed Faraday rotation takes place internally to the radio lobes. If the Faraday rotation associated with NGC 612 is taking place inside the lobes of the radio galaxy, it would be one of only a few objects (e.g. O'Sullivan et al. 2013) that have been shown to have this distribution of magneto-ionic material. It should be noted that the work carried out by O'Sullivan et al. (2013) was over a more limited frequency range (1288–1480 MHz) with more sparse sampling across the imaged bandwidth. As polarization work towards multiple radio sources has yet to be carried out over as large of a band as the work presented here, it is possible that the detection of internal Faraday rotation could become more frequent towards large radio lobes.

Assuming that the lobes are threaded with thermal, magneto-ionic material, it is possible to approximate the amount of thermal material that needs to be diffused in the lobes of NGC 612 to produce the observed signal. Using the definition of Faraday depth from Burn (1966),

$$\phi(L) = 0.812 \int_L^0 n_e B_\parallel \mathrm{d}l, \tag{9}$$

we can solve for the free electron density (n_e). We take L to be the effective distance through the magneto-ionic material in parsecs, that is the path-length (l) times the filling factor of ionized gas along the total line of sight (f) (Reynolds 1991). Using our previous assumed values for the path-length (l), filling factor (f), and $B_\parallel$ (Section 6.1), we calculate an implied density of $n_e \sim 1.8 \times 10^{-5}\,\mathrm{cm^{-3}}$. The radio lobes can be roughly resemble two cylinders, each with a radius of 70 kpc and lengths of 160 and 220 kpc for the eastern and western lobes, respectively. This geometry implies a total volume of the radio emission of $V \sim 2 \times 10^{71}\,\mathrm{cm^3}$. Were this volume to be uniformly filled with the above calculated n_e, it follows that the implied thermal mass within the lobes would be $M_{\mathrm{th}} \sim n_e m_H f V \sim 2.5 \times 10^8\,\mathrm{M_\odot}$ where m_H is the mass of ionized hydrogen. We note that this estimate depends heavily on the numerous assumptions that we have made.

It is possible that thermal material was entrained from the galaxy as the jet pushed its way through the galactic disc (Laing & Bridle 2002). If we assume an age for the radio lobes of 0.1 Gyr (Blundell & Rawlings 2000; Parma et al. 2002), the lobes of NGC 612 would need to entrain an average amount of $\sim 2.5\,\mathrm{M_\odot\,yr^{-1}}$. This estimate is a few orders of magnitude larger than the amount needed to decelerate relativistic jets (Bicknell 1994; Laing & Bridle 2002) and it is unlikely that entrainment is the sole origin for the bulk of the thermal material. It is more likely that the bulk of the magneto-ionic plasma responsible for the observed Faraday rotation signal has been accumulated by a combination of the mechanisms discussed (e.g. thin skin, Faraday eddies, and entrainment).

6.4 The hotspot

The area surrounding the hotspot in the eastern lobe offers an intriguing polarization signal. In this region, dispersion levels are strongest (Fig. 11) and the Faraday depth sign is opposite to that of the majority of the radio galaxy (Fig. 10). At this particular location, NGC 612 is interacting with its neighbouring galaxy NGC 619 via a tenuous H I bridge (Emonts et al. 2008).

Depolarization can be caused by change in strength or direction of the coherent magnetic field. It is therefore possible that the observed depolarization is due to an increase in the turbulence of the magnetic field as the jet of NGC 612 is ploughing into the tidal bridge. However, this increase in random motion would not give rise to a sign change in the coherent magnetic field direction. Furthermore, Fig. 9 shows that the intrinsic polarization angle near the hotspot does not have a significant change in orientation, insinuating that the corresponding sign-change in Faraday depth does not come about due to a characteristic change in the geometry of the synchrotron plasma. Explaining the change from positive to negative Faraday depth may require additional factors.

One possibility is that there exists an intervening cloud of magnetized gas along the line of sight associated with the hotspot. Emonts et al. (2008) detect a faint bridge of H I material spanning the distance between NGC 612 and neighbouring galaxy NGC 619. Recent works by Banfield et al. (2017) use the contrast between the hotspot and the larger diffuse lobes as evidence of a strong interaction of the radio galaxy with its surrounding environment. If this bridge, which is believed to be tidal in origin, were to host a coherent line-of-sight magnetic field oriented opposite that of NGC 612, the observed Faraday depth associated with this region would appear opposite to the bulk of NGC 612 if the magnetic field in the H I cloud were sufficiently negative.

There have been numerous detections of magnetized, tidally stripped material associated with continuum bridges (e.g. Condon et al. 1993; Nikiel-Wroczyński et al. 2013; Basu et al. 2017) as well as neutral H I tidal features (Hill, Haffner & Reynolds 2009; McClure-Griffiths et al. 2010; Kaczmarek et al. 2017). The existence of a coherent magnetic field in the H I cloud could provide structural support against the intruding AGN jet, resulting in a longer

lifetime for the tidal remnant. Higher resolution observations of the polarized signal associated with the HS, in addition to information on the free-electron density in the H I cloud, are needed to explore this region further.

7 CONCLUSIONS

We have presented a spectropolarimetric study of the radio galaxy NGC 612 using broad-band observations covering 1.3–3.0 GHz taken with the ATCA. It is immediately evident that the polarization signal depends upon the position within the lobes. We have demonstrated that majority of the polarization signal seen associated with the radio lobes can be explained through a single polarization component, although the exact mechanism remains unclear because of similarity between model fits. Using *qu*-fitting, we were able to confidently recover the intrinsic polarization properties associated with the lobes.

We have explored any environmental implications from the observed Faraday depth signal. While we cannot rule out the entrainment of thermal material from the galactic disc, we find evidence of Faraday eddies on the surface of the synchrotron lobes, as seen by a sinusoidal variation in Faraday depth as a function of distance along the lobe. We argue that these surface waves are formed via the expansion of the synchrotron lobes into the surrounding medium, forming a thin skin ($dl \sim 20$ kpc) of thermal material that is responsible for the bulk of the observed Faraday rotation.

We estimate a total minimum magnetic field strength of $B_{\rm min} \sim 4.2$ μG in the lobes of NGC 612. If the thermal material is distributed as a thin skin, we calculate a free-electron density in the skin of order $n_e \sim 10^{-4}$ cm^{-3}, assuming equipartition. As NGC 612 is embedded in a halo of hot, X-ray emitting plasma, we argue that achieving this density would require little compression of the ambient IGrM.

We observe intriguing Faraday signal at the location of the hotspot in the east lobe of NGC 612. At this location, a H I cloud, arising from a previous interaction, has been observed. We hypothesize that this signal might be explained if the tidal material is threaded with a coherent magnetic field, oriented in the opposite direction to the bulk of the Faraday rotating material. Future high-resolution polarization observations, in addition to path-length estimates, are needed to confirm this hypothesis.

In order to correctly account for any spectral dependencies that may be associated with the two jets or the compact hotspot in the lobes, follow-up, high-resolution radio polarization observations are required. Furthermore, high-resolution follow-up observations have the potential to break the ambiguity between our modelling results, in that they may resolve smaller surface features, that are predicted by our assumed thin skin model, which have been smoothed by our synthesized beam. Such an observational approach would be advantageous for all future related studies. The early science stages of the Australian Square Kilometre Array Pathfinder will provide additional λ^2-coverage allowing for the resolution of all Faraday components along the line of sight, making it easier to deduce the true polarization mechanisms responsible for the observed signal. Better electron density estimates of the intragroup medium and magnetic field estimates will strengthen further analysis of the NGC 612 system and should be possible with sensitive X-ray observations, such as those offered with the *XMM–Newton* telescope.

ACKNOWLEDGEMENTS

The Australia Telescope Compact Array is part of the Australia Telescope National Facility that is funded by the Australian Government for operation as a National Facility managed by CSIRO. We thank the staff at the Australia Telescope Compact array for their assistance and support with this project. We also appreciate the invaluable insight offered to us by R. W. Hunstead, R. A. Laing, and L. Rudnick. B.M.G. and C.R.P acknowledge the support of the Australian Research Council through grant no. FL100100114. The Dunlap Institute is funded through an endowment established by the David Dunlap family and the University of Toronto. N.M.M.-G. acknowledges the support of the Australian Research Council through Future Fellowship FT150100024. X.H.S. is supported by the National Natural Science Foundation of China under grant no. 11763008.

REFERENCES

Aguirre A., Hernquist L., Schaye J., Katz N., Weinberg D. H., Gardner J., 2001, ApJ, 561, 521
Anderson C. S., Gaensler B. M., Heald G. H., O'Sullivan S. P., Kaczmarek J. F., Feain I. J., 2017, ApJ
Banfield J. K., O'Sullivan S. O., Wieringa M. H., Emonts B. H. C., 2017, MNRAS, in press
Basu A., Mao S. A., Kepley A. A., Robishaw T., Zweibel E. G., Gallagher J. S., III, 2017, MNRAS, 464, 1003
Beck R., Krause M., 2005, Astron. Nachr., 326, 414
Begelman M. C., Cioffi D. F., 1989, ApJ, 345, L21
Begelman M. C., Blandford R. D., Rees M. J., 1984, Rev. Mod. Phys., 56, 255
Bicknell G. V., 1994, Aust. J. Phys., 47, 669
Bicknell G. V., Cameron R. A., Gingold R. A., 1990, ApJ, 357, 373
Blundell K. M., Rawlings S., 2000, AJ, 119, 1111
Bolton J. G., Shimmins A. J., 1973, Aust. J. Phys. Astrophys. Suppl., 30, 1
Bonafede A., Feretti L., Murgia M., Govoni F., Giovannini G., Dallacasa D., Dolag K., Taylor G. B., 2010, A&A, 513, A30
Brentjens M. A., de Bruyn A. G., 2005, A&A, 441, 1217
Burn B. J., 1966, MNRAS, 133, 67
Churazov E., Brüggen M., Kaiser C. R., Böhringer H., Forman W., 2001, ApJ, 554, 261
Condon J. J., Helou G., Sanders D. B., Soifer B. T., 1993, AJ, 105, 1730
Croston J. H., Hardcastle M. J., Harris D. E., Belsole E., Birkinshaw M., Worrall D. M., 2005, ApJ, 626, 733
de Vaucouleurs G., de Vaucouleurs A., Corwin H. G., Jr, Buta R. J., Paturel G., Fouqué P., 1991, Third Reference Catalogue of Bright Galaxies, Volume I: Explanations and references, Volume II: Data for galaxies between 0^h and 12^h, Volume III: Data for galaxies between 12^h and 24^h
Eguchi S., Ueda Y., Awaki H., Aird J., Terashima Y., Mushotzky R., 2011, ApJ, 729, 31
Ekers R. D., Goss W. M., Kotanyi C. G., Skellern D. J., 1978, A&A, 69, L21
Emonts B. H. C., Morganti R., Oosterloo T. A., Holt J., Tadhunter C. N., van der Hulst J. M., Ojha R., Sadler E. M., 2008, MNRAS, 387, 197
Ensslin T. A., Vogt C., Clarke T. E., Taylor G. B., 2003, ApJ, 597, 870
Fanaroff B. L., Riley J. M., 1974, MNRAS, 167, 31P
Fomalont E. B., 1968, ApJS, 15, 203
Fomalont E. B., Ebneter K. A., van Breugel W. J. M., Ekers R. D., 1989, ApJ, 346, L17
Foreman-Mackey D., Hogg D. W., Lang D., Goodman J., 2013, PASP, 125, 306
Gopal-Krishna Wiita P. J., 2000, A&A, 363, 507
Gourgouliatos K. N., Braithwaite J., Lyutikov M., 2010, MNRAS, 409, 1660
Govoni F. et al., 2010, A&A, 522, A105
Guidetti D., Laing R. A., Murgia M., Govoni F., Gregorini L., Parma P., 2010, A&A, 514, A50

Guidetti D., Laing R. A., Bridle A. H., Parma P., Gregorini L., 2011, MNRAS, 413, 2525
Guidetti D., Laing R. A., Croston J. H., Bridle A. H., Parma P., 2012, MNRAS, 423, 1335
Haves P., 1975, MNRAS, 173, 553
Hill A. S., Haffner L. M., Reynolds R. J., 2009, ApJ, 703, 1832
Holt J., Tadhunter C. N., González Delgado R. M., Inskip K. J., Rodriguez Zaurin J., Emonts B. H. C., Morganti R., Wills K. A., 2007, MNRAS, 381, 611
Kaczmarek J. F., Purcell C. R., Gaensler B. M., McClure-Griffiths N. M., Stevens J., 2017, MNRAS, 467, 1776
Kotanyi C. G., Ekers R. D., 1979, A&A, 73, L1
Kronberg P. P., Bernet M. L., Miniati F., Lilly S. J., Short M. B., Higdon D. M., 2008, ApJ, 676, 70
Laing R. A., 1988, Nature, 331, 149
Laing R. A., Bridle A. H., 2002, MNRAS, 336, 1161
Laing R. A., Bridle A. H., Parma P., Murgia M., 2008, MNRAS, 391,521
Mauch T., Murphy T., Buttery H. J., Curran J., Hunstead R. W., Piestrzynski B., Robertson J. G., Sadler E. M., 2003, MNRAS, 342, 1117
McClure-Griffiths N. M., Madsen G. J., Gaensler B. M., McConnell D., Schnitzeler D. H. F. M., 2010, ApJ, 725, 275
McNamara B. R., Kazemzadeh F., Rafferty D. A., Bîrzan L., Nulsen P. E. J., Kirkpatrick C. C., Wise M. W., 2009, ApJ, 698, 594
Mills B. Y., Slee O. B., Hill E. R., 1960, Aust. J. Phys., 13, 676
Morganti R., Killeen N. E. B., Tadhunter C. N., 1993, MNRAS, 263, 1023
Mulchaey J. S., Zabludoff A. I., 1998, ApJ, 496, 73
Nikiel-Wroczyński B., Soida M., Urbanik M., Beck R., Bomans D. J., 2013, MNRAS, 435, 149
O'Sullivan S. P. et al., 2012, MNRAS, 421, 3300
O'Sullivan S. P. et al., 2013, ApJ, 764, 162
Oppermann N. et al., 2015, A&A, 575, A118
Owen F. N., Laing R. A., 1989, MNRAS, 238, 357
Owen F. N., White R. A., 1991, MNRAS, 249, 164
Parma P., Murgia M., de Ruiter H. R., Fanti R., 2002, New A Rev., 46, 313
Raimann D., Storchi-Bergmann T., Quintana H., Hunstead R., Wisotzki L., 2005, MNRAS, 364, 1239
Ramella M., Geller M. J., Pisani A., da Costa L. N., 2002, AJ, 123, 2976
Reuland M. et al., 2007, AJ, 133, 2607
Reynolds R. J., 1991, in Bloemen H., ed., Proc. IAU Symp. 144, The Interstellar Disk-Halo Connection in Galaxies. Springer-Verlag, Dordrecht, the Netherlands, p. 67
Rudnick L., Blundell K. M., 2003, ApJ, 588, 143
Sault R. J., Cornwell T. J., 1999, in Taylor G. B., Carilli C. L., Perley R. A., eds, ASP Conf. Ser. Vol. 180, Synthesis Imaging in Radio Astronomy II, A Collection of Lectures from the Sixth NRAO/NMIMT Synthesis Imaging Summer School. Astron. Soc. Pac., San Francisco, p. 657
Sault R. J., Teuben P. J., Wright M. C. H., 1995, in Shaw R. A., Payne H. E., Hayes J. J. E., eds, ASP Conf. Ser. Vol. 77, Astronomical Data Analysis Software and Systems IV. Astron. Soc. Pac., San Francisco, p. 433
Schilizzi R. T., McAdam W. B., 1975, MmRAS, 79, 1
Simard-Normandin M., Kronberg P. P., Button S., 1981, ApJS, 45, 97
Sokoloff D. D., Bykov A. A., Shukurov A., Berkhuijsen E. M., Beck R., Poezd A. D., 1998, MNRAS, 299, 189
Stil J. M., Taylor A. R., Sunstrum C., 2011, ApJ, 726, 4
Sun M., 2012, New J. Phys., 14, 045004
Tadhunter C. N., Morganti R., di Serego-Alighieri S., Fosbury R. A. E., Danziger I. J., 1993, MNRAS, 263, 999
Tashiro M., Makishima K., Kaneda H., 2000, Adv. Space Res., 25, 751
Wall J. V., Schilizzi R. T., 1979, MNRAS, 189, 593
Wilson W. E. et al., 2011, MNRAS, 416, 832
Xu H., Li H., Collins D. C., Li S., Norman M. L., 2010, ApJ, 725, 2152

APPENDIX A: POLARIZATION PARAMETER AND UNCERTAINTY MAPS

In Section 5, we have argued that each of the single-component polarization models discussed in this work offers similar goodness of fit to the observed polarization spectra. Below, we present each of the parameter maps returned from our model-fitting routine. The agreement in parameter values between all models adds credence to the data validity. We point out that the major discrepancies between the parameter maps lie in the maps of Faraday depth, in that in the case of internal Faraday rotation, the total Faraday depth is equal to two times the observed Faraday rotation ($\phi = \frac{1}{2}$RM).

We also present the corresponding uncertainty maps represent the average of the 1σ deviations of the walkers above and below the resultant best fit (σ_+ and σ_-, respectively). Figs A1 and A2 correspond to the parameter and uncertainty maps for the Faraday thin model, and Figs A3 and A4 to the external Faraday dispersion model. Parameter and uncertainty maps corresponding to the differential Faraday rotation model are given in Figs A5 and A6, respectively. Figs A7 and A8 represent the parameter and uncertainty maps for the internal Faraday dispersion model.

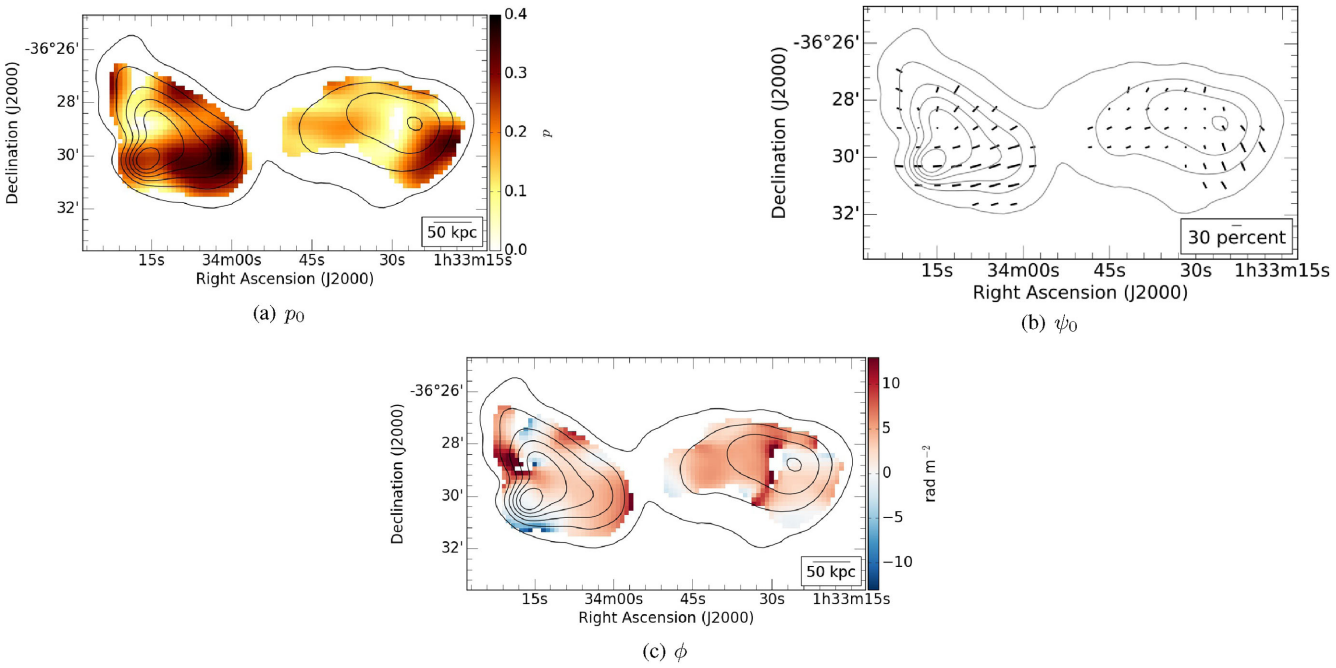

(a) p_0 (b) ψ_0 (c) ϕ

Figure A1. Faraday thin parameter maps showing intrinsic polarization (a), intrinsic polarization angle (b), and Faraday depth (c). The length of each vector in Fig. (b) represents the corresponding polarization fraction at that location. Each subfigure has a scale bar in the lower right-hand corner. Total intensity contours mark 25–400 mJy beam^{-1} every 75 mJy beam^{-1}.

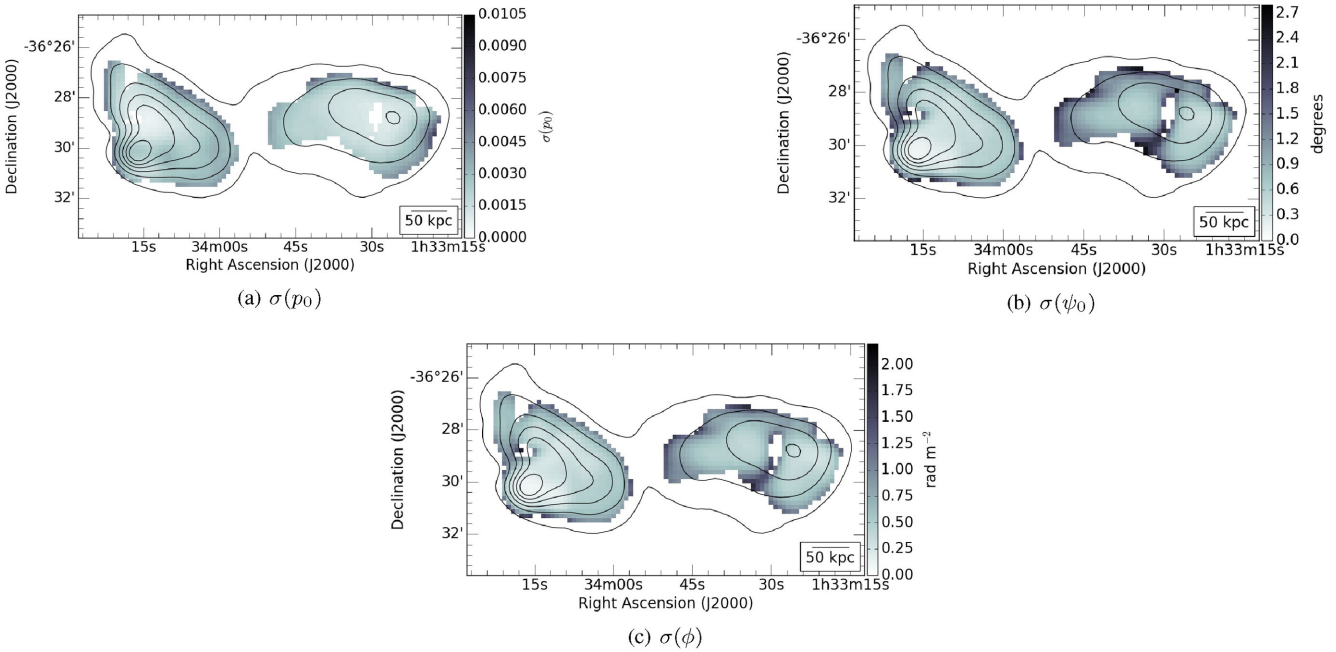

(a) $\sigma(p_0)$ (b) $\sigma(\psi_0)$ (c) $\sigma(\phi)$

Figure A2. Uncertainty maps for a Faraday thin model. Maps shown correspond to uncertainty in intrinsic polarization fraction (a), uncertainty in intrinsic polarization angle, in degrees (b), and uncertainty in Faraday depth (c). Each subfigure has a scale bar in the lower right-hand corner. Total intensity contours mark 25–400 mJy beam^{-1} every 75 mJy beam^{-1}.

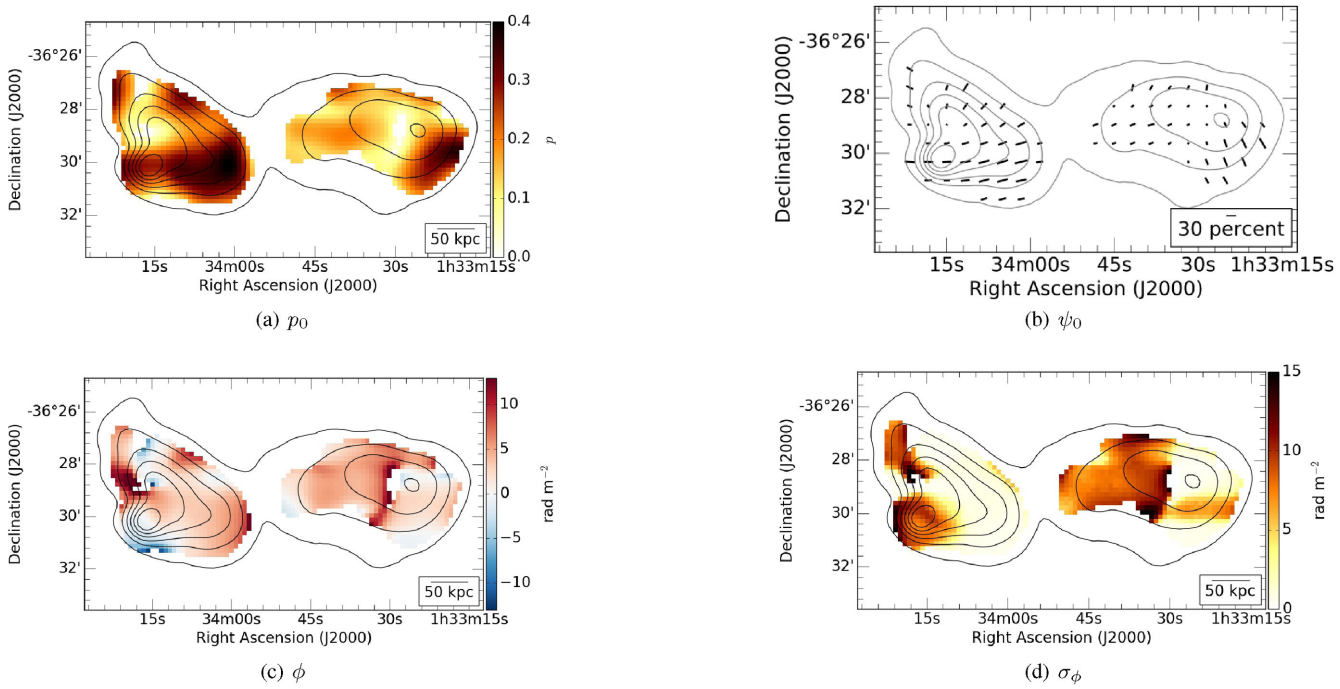

(a) p_0 (b) ψ_0 (c) ϕ (d) σ_ϕ

Figure A3. EFD parameter maps showing intrinsic polarization (a), intrinsic polarization angle (b), Faraday depth (c), and Faraday dispersion (d). The length of each vector in Fig. (b) represents the corresponding polarization fraction at that location. Each subfigure has a scale bar in the lower right-hand corner. Total intensity contours mark 25–400 mJy beam^{-1} every 75 mJy beam^{-1}.

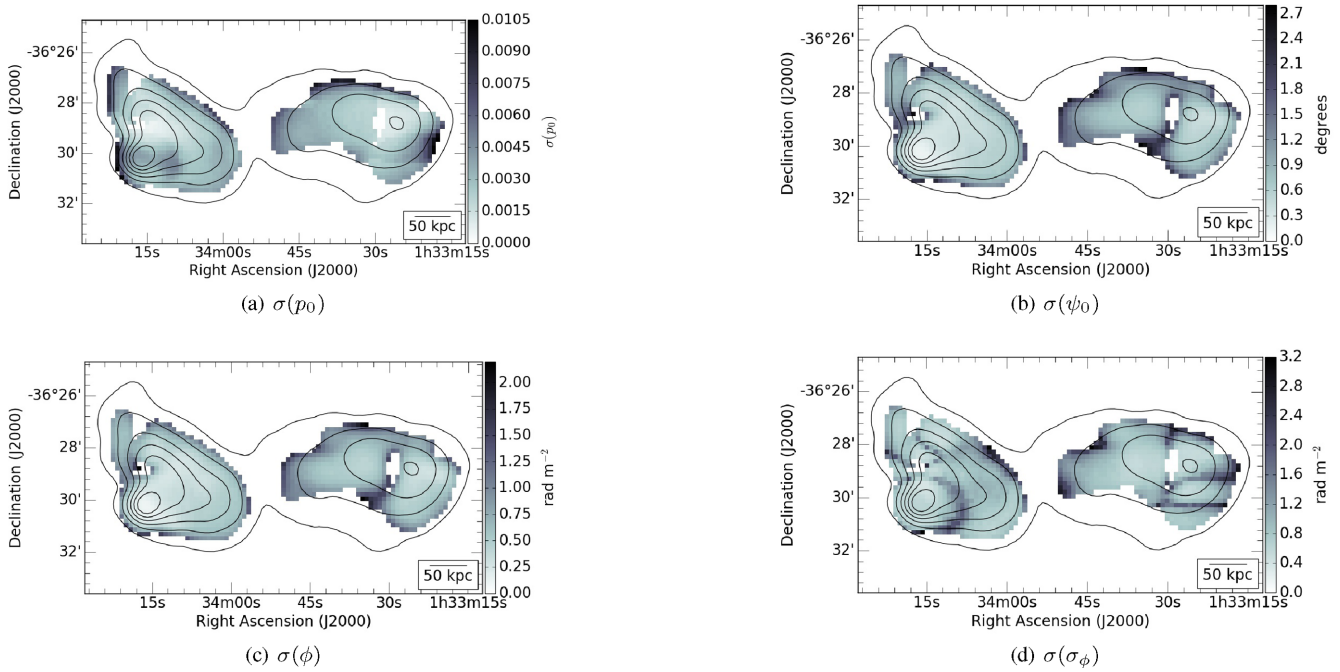

(a) $\sigma(p_0)$ (b) $\sigma(\psi_0)$ (c) $\sigma(\phi)$ (d) $\sigma(\sigma_\phi)$

Figure A4. Uncertainty maps pertaining to the EFD polarization model. The figures shown represent uncertainty in intrinsic polarization (a), uncertainty in the intrinsic polarization angle (b), uncertainty in Faraday depth (c), and uncertainty in the Faraday dispersion (d). Each subfigure has a scale bar in the lower right-hand corner. Total intensity contours mark 25–400 mJy beam^{-1} every 75 mJy beam^{-1}.

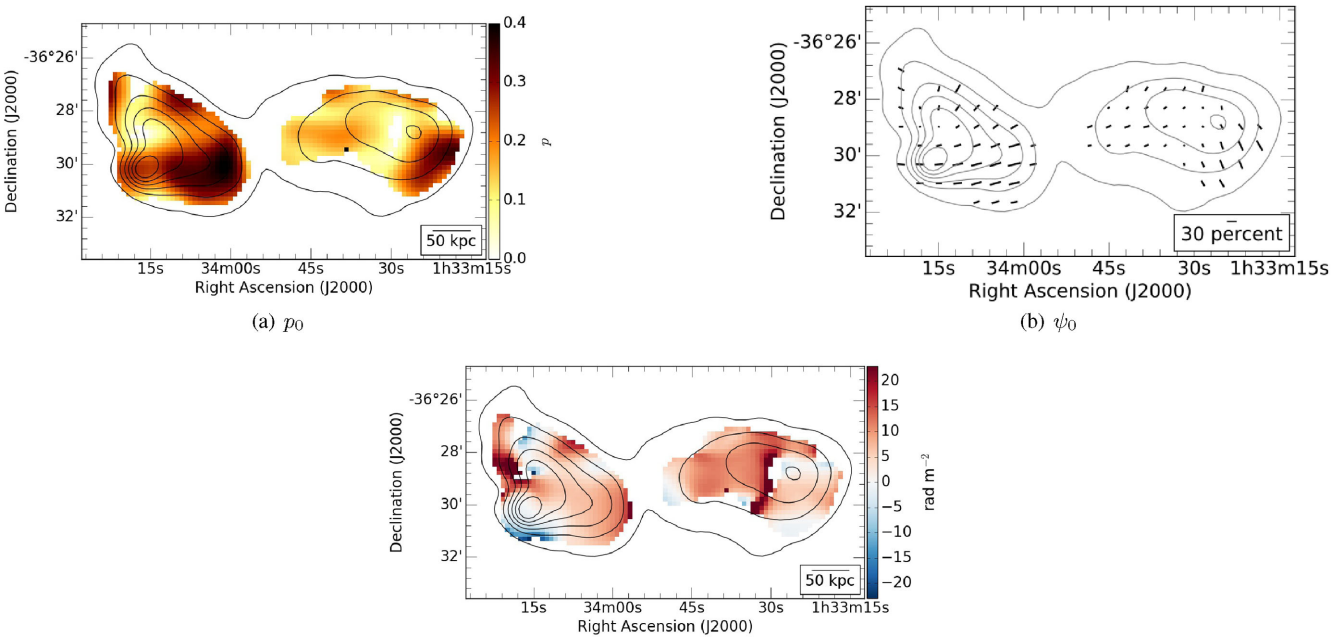

(a) p_0 (b) ψ_0 (c) ϕ

Figure A5. Parameter maps corresponding to the DFR polarization model showing intrinsic polarization (a), intrinsic polarization angle (b), and Faraday depth (c). The length of each vector in Fig. (b) represents the corresponding polarization fraction at that location. Each subfigure has a scale bar in the lower right-hand corner. Total intensity contours mark 25–400 mJy beam^{-1} every 75 mJy beam^{-1}.

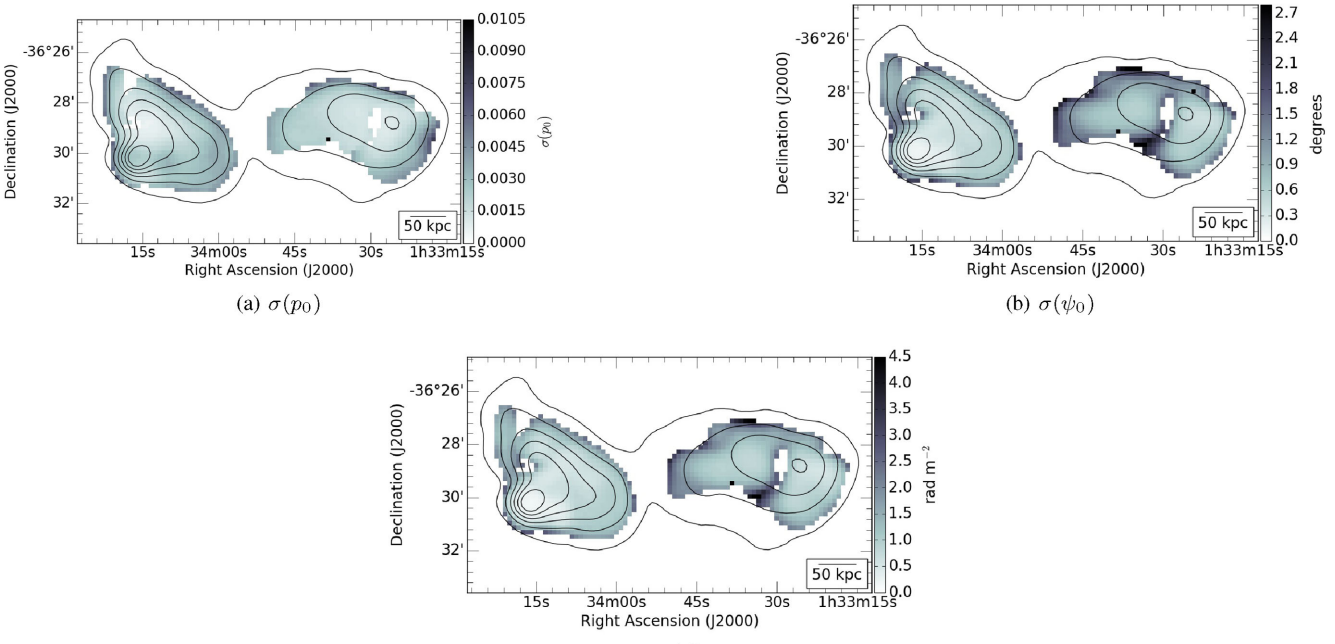

(a) $\sigma(p_0)$ (b) $\sigma(\psi_0)$ (c) $\sigma(\phi)$

Figure A6. Parameter uncertainty maps corresponding to the DFR polarization model. Uncertainties shown are for intrinsic polarization (a), intrinsic polarization angle (b), and Faraday depth (c). Each subfigure has a scale bar in the lower right-hand corner. Total intensity contours mark 25–400 mJy beam^{-1} every 75 mJy beam^{-1}.

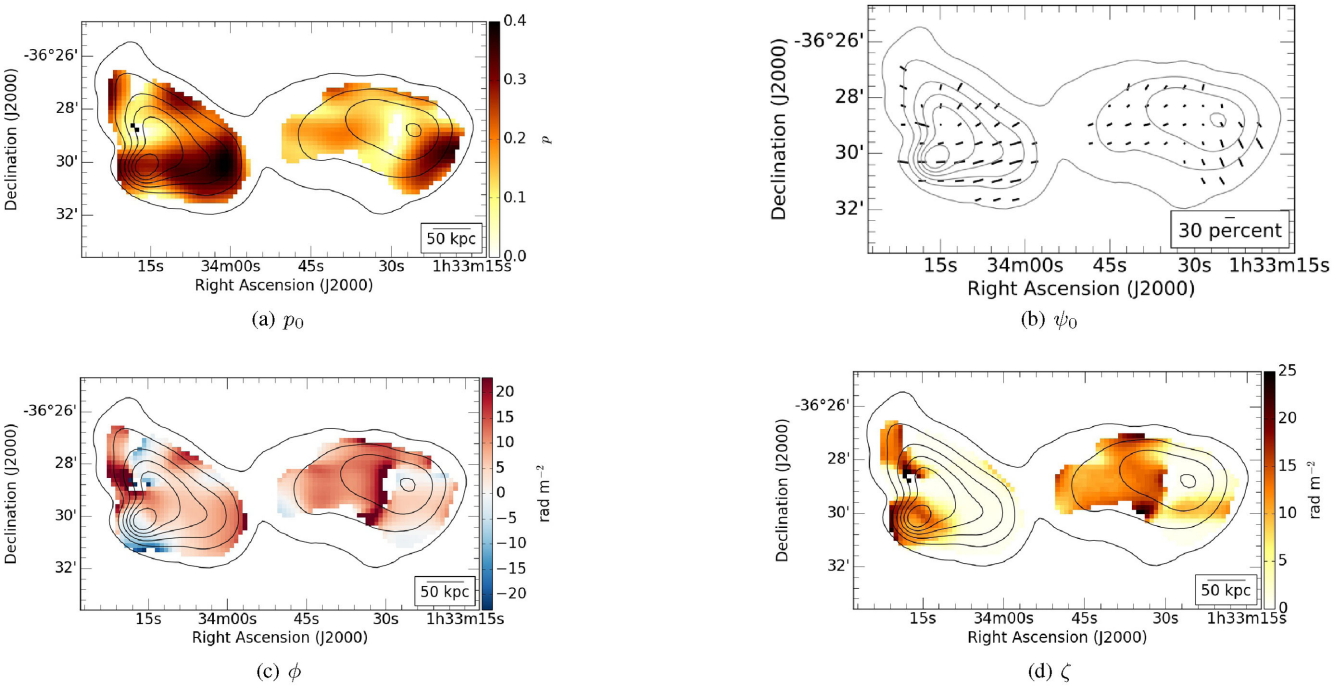

Figure A7. Parameter maps corresponding to the IFD polarization model showing intrinsic polarization (a), intrinsic polarization angle (b), Faraday depth (c), and internal Faraday dispersion (d). The length of each vector in Fig. (b) represents the corresponding polarization fraction at that location. Each subfigure has a scale bar in the lower right-hand corner. Total intensity contours mark 25–400 mJy beam^{-1} every 75 mJy beam^{-1}.

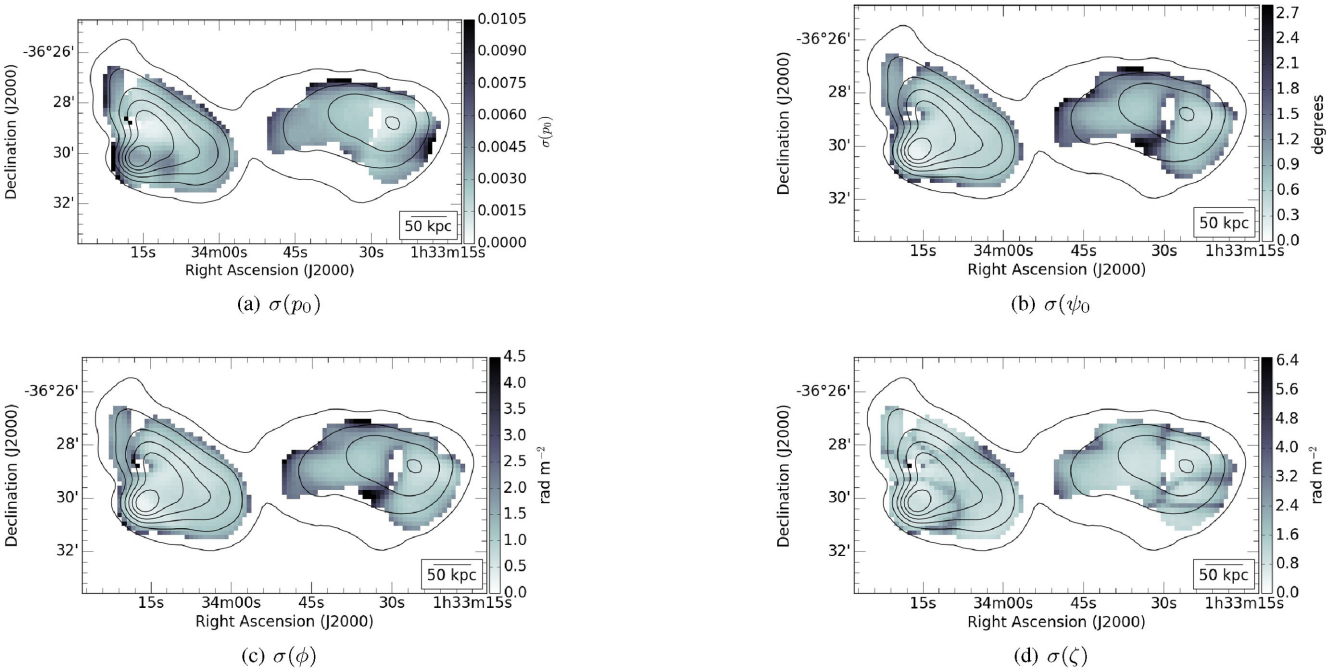

Figure A8. Parameter uncertainty maps corresponding to the IFD polarization model. Uncertainties shown are for intrinsic polarization (a), intrinsic polarization angle (b), Faraday depth (c), and Faraday dispersion (d). Each subfigure has a scale bar in the lower right-hand corner. Total intensity contours mark 25–400 mJy beam^{-1} every 75 mJy beam^{-1}.

This paper has been typeset from a TEX/LATEX file prepared by the author.